August 2020

# Cell-adhesion Activities Responding to Nano-Dynamic Substrate

Huaiyu Shi
*Syracuse University*

# Abstract

Focal adhesions are the large molecular complexes that anchor cells to the ECM, which is involved in cell spreading, migration, and proliferation. In our previous work, the study of cardiomyocyte morphological changes and myofibril remodeling, responding to the dynamic nano-topographic substrate, have been accomplished. The results showed focal adhesion experienced disassembly and reassembly in the first 12 hours. In this study, the hiPSC-CMs were seeded on the SMP substrates with the flat-to-wrinkle dynamic surface. Paxillin, vinculin, and zyxin from different layers of focal adhesive architectures were co-stained with F-actin. The fluorescent images were analyzed to investigate the details of focal adhesions remodeling and the dynamics of costameres in the first stage post triggering the substrate wrinkle formation.



**Keywords**: Mechanobiology, Cardiomyocyte, Focal adhesion, Shape memory polymer, Dynamic substrate

# Cell-adhesion Activities Responding to Nano-Dynamic Substrate

By

**Huaiyu Shi**

B.S. Biological Science, Tianjin Normal University, China, 2015

M.S. Genetics, Tianjin University, China, 2018

**Thesis**

Submitted in partial fulfillment of the requirements for the degree of

Master of Sciences (M.S.) in *Bioengineering*

**Syracuse University**

**August 2020**

# Table of Contents

# List of Figures

# 1. Introduction

## 1.1. Cardiomyocyte Structure and Organization

### 1.1.1. Cardiomyocytes

Cardiomyocytes are muscle cells that only exist in hearts. Like skeletal muscle, cardiomyocyte is a kind of striated muscle that has myofibers composed by repeated functional unit called sarcomere. The actin and myosin form thin filament and thick filament, respectively, within the sarcomere, which enables the contraction of the muscle cell. The developmental program of cardiac muscle tissue is the result, and it is driven by the complexity of extracellular matrix (ECM) interaction, non-cardiomyocyte interactions, mechanical stimuli, etc. With the maturation of cardiomyocyte, the morphology of cell changes from round shape in early fetal and late fetal stages to elongated rod shape[1,2] (**Figure 1**). Meanwhile, the surface area of cardiomyocytes increased largely from 1,000-1,300 $\mu m^2$ to 10,000-14,000 $\mu m^2$[3]. In neonatal cardiomyocytes and adult cardiomyocytes, the cells are more aligned compare to either fetal stage. The better alignment enhances the conduction of electrical signals between cells, which augment tissue contractility[4,5].

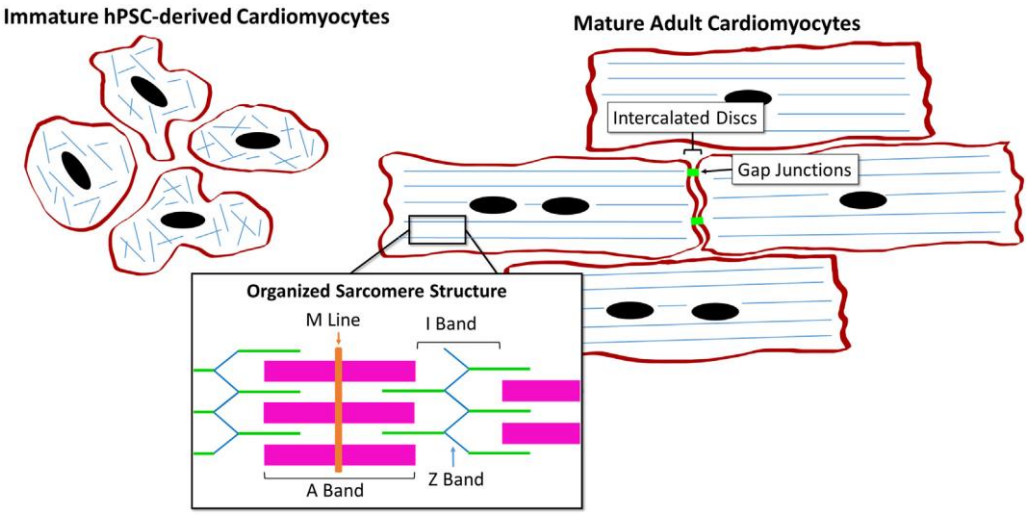


**Figure 1** Maturity of cardiomyocytes. Human induced pluripotent stem cell (hiPSC)-derived cardiomyocytes (left) and adult cardiomyocytes (right) demonstrating the structural and organizational changes during maturation[6].

### 1.1.2. Focal adhesions

Cells need to anchor to the ECM to keep the appropriate morphologies and functionalities. These anchors are mediated by cell-matrix adhesion junctions. Focal adhesions, the assembly of multiple proteins serving as the linkage, are responsible for the mechanical signal transmitting between cells and the ECM. Under the observation of immunofluorescence microscopy, focal adhesions are bar-shaped structures clustering at the end of cytoskeleton actin filaments and myofibers[7]. The structures and various focal adhesion components have hardly been analyzed completely. In 2010, Kanchanawang et al. demonstrated the three-dimensional architecture of focal adhesions by utilizing interferometric photoactivation and localization microscopy, and photoactivation fusion proteins[8]. In nanoscale, the organization of focal adhesions can be mainly divided into three layers: the outermost signaling layer, containing integrins, focal adhesion kinase (FAK), and paxillin, penetrates the plasma membrane of a cell and directly forms the attachment to ECM; the innermost layer, containing α-actinin, zyxin, and vasodilator-stimulated phosphoprotein, connects with actin

bundles; and a force-transduction layer, containing vinculin and talin, lays intermediately and isolates integrin layer and actin layer with a distance of 40 nm **(Figure 2)**.

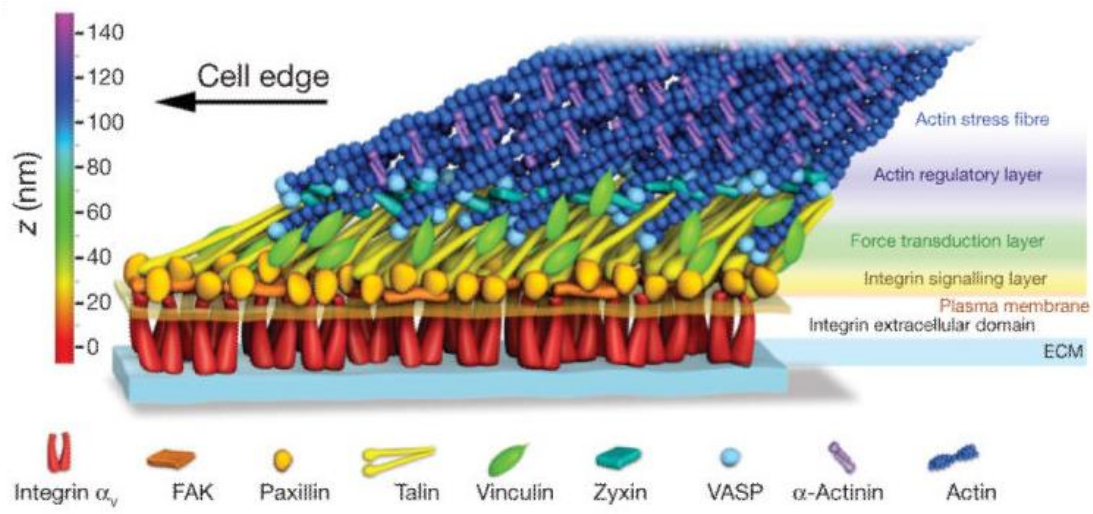


**Figure 2** Schematic model of the focal adhesion complex[9].

Focal adhesions are involved in cell migration, cell proliferation, and mechanical signaling, etc. The two-dimensional migration of cells relies on the dynamics of focal adhesion turnover. This process can be described as a classical model with three steps: protrusion of cell leading edge form lamellipodium; assembly of new focal adhesions enhances the cell attachment in the leading edge; focal adhesions disassemble in trailing edge, which helps cell achieve the migration[10]. Talin has been proven to be induced during striated muscle differentiation and the absence of β1 integrin impairs the differentiation of cardiac muscle cells[11,12]. The stability of focal adhesions affected by the activation of FAK regulates the paxillin nuclear transport, which is highly associated with the proliferation of various cancer cells[13]. Nardone et al. found that YAP controlled by the modification of ECM regulated the formation of focal adhesions transcriptionally, which further determined the cell mechanics[14].

In 2018, Dylan T. Burnette found that the stabilization of focal adhesions enables an earlier

recruitment of α-actinin-2 to form Z-bodies in the edge of a cell and accelerated the maturation of myofibrils. The stabilized focal adhesion might allow greater coupling of myofibrils with the ECM and, therefore, slowing the retrograde movement of muscle stress fibers[15]. Focal adhesions have been reported as the initial sites for the formation of costameres and several focal adhesion components are highly associated in the sarcomere formation. Vinculin, the protein existing in the force transduction layer of focal adhesion complexes is a prerequisite for the mature sarcomere formation[16]. Also, the activation of FAK caused by autophosphorylation is necessary for the reorganization of sarcomeres[17,18].

### 1.1.3. Costameres

Sharing many structural features like focal adhesions, the costameres are another set of cell-matrix adhesions that can only be found in striated muscle. Originally, the term costamere was used to describe a vinculin-containing cortical lattice in muscle cells[19]. In cardiomyocytes, costameres are rib-like subcellular structures aligning with the Z-line of sarcomeres[20] **(Figure 3)**. Dystrophin glycoprotein complexes and integrin-vinculin-talin complexes are two major costameric complexes reported to link the Z-line with ECM through sarcolemma **(Figure 4)**. Costameres, serving as the linkages between sarcomeres and ECM, master the conduction of contractile force generated from sarcomeres to ECM and sense the external force from ECM to the cells[21,22]. Thus, it is rational to expect that the stabilization and integrity of costamere structures are pivotal for the normal contraction of muscle cells.

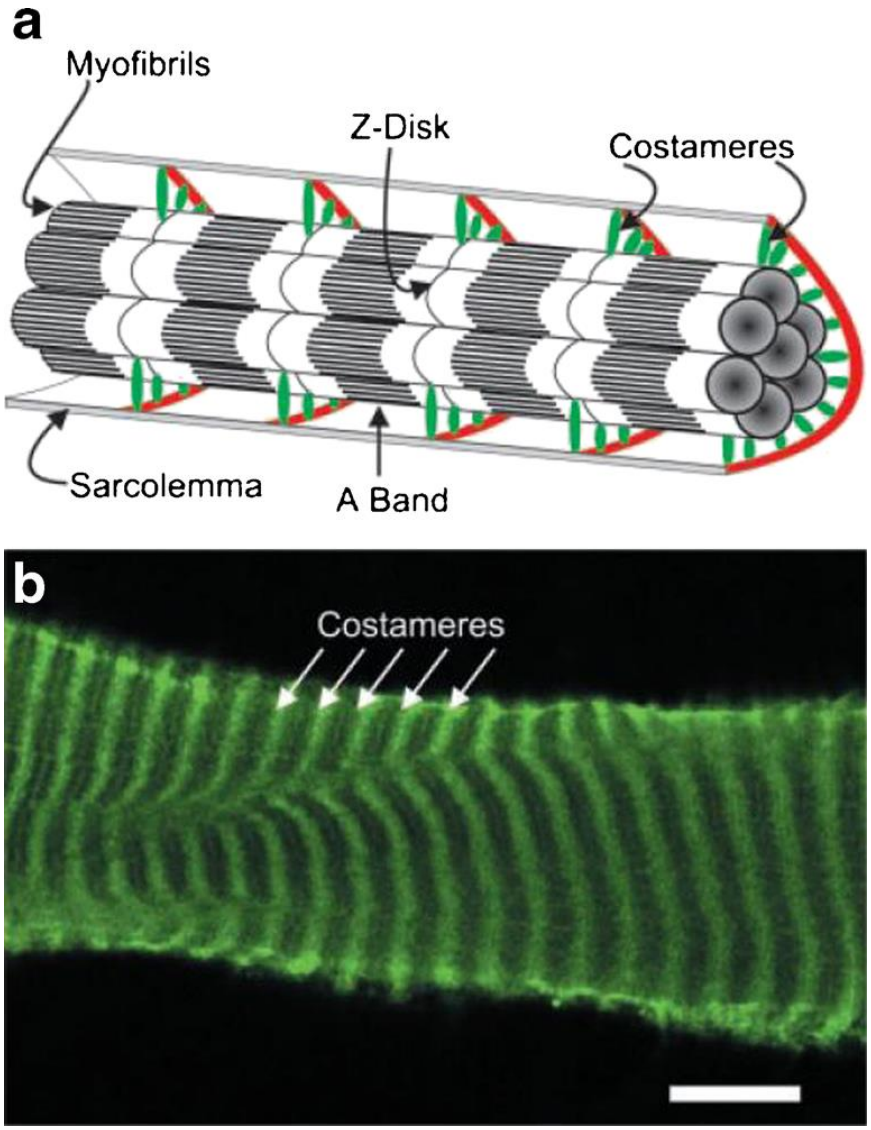


**Figure 3** Location of costameres in striated muscle. A, schematic diagram indicating that costameres are sites anchor z-discs of sarcomeres to sarcolemma. B, costameric γ-actin staining showing striated pattern on normal sarcolemma. Scale bar, 10 μm[23].

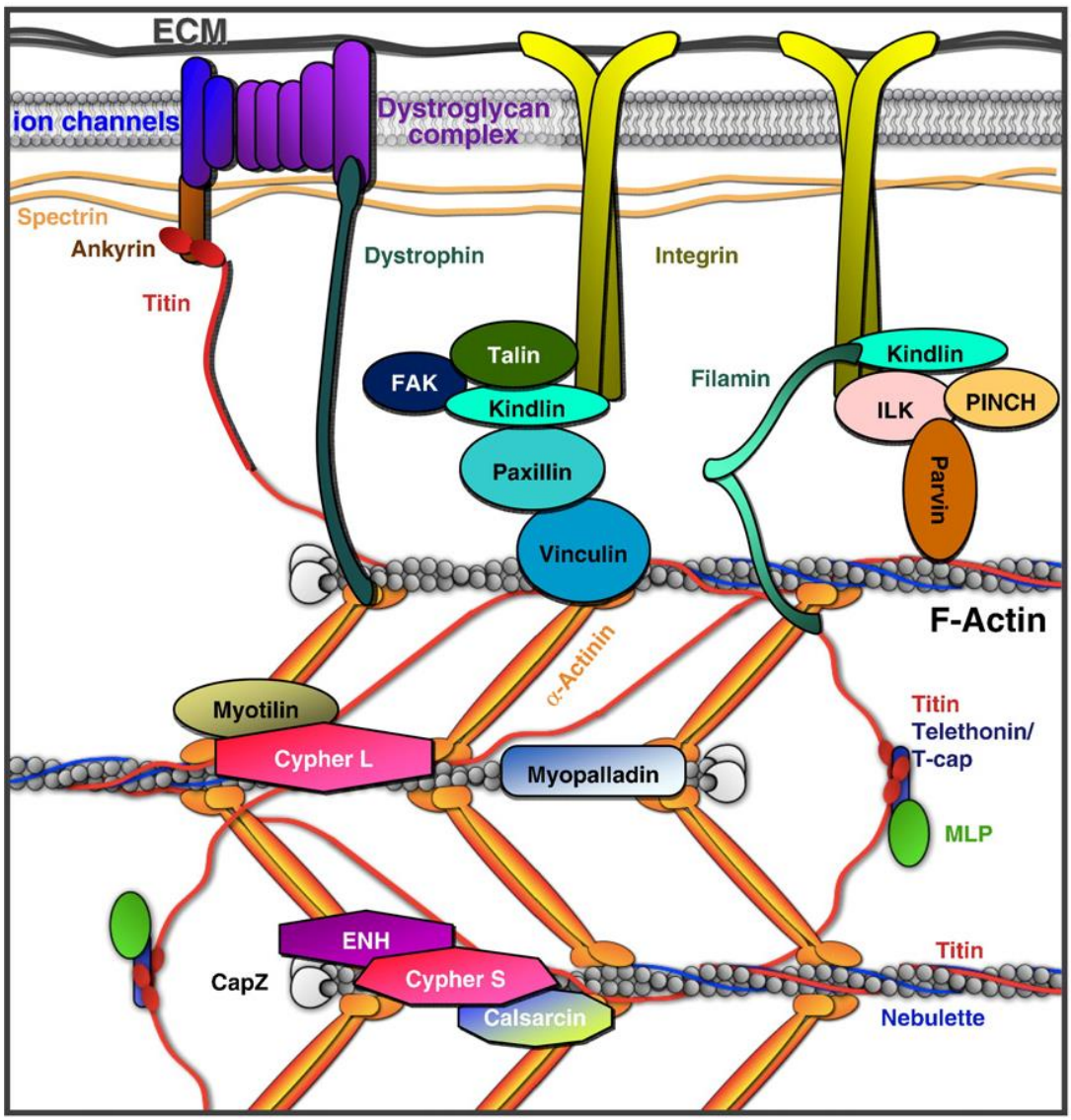


**Figure 4** Costamere protein complex anchoring Z-discs to ECM through membrane. Dystrophin glycoprotein complex and integrin-vinculin-talin complex are two major costameric complexes[24].

In addition to mechanotransduction, costameres are associated with the *de novo* assembly of sarcomeres. During the initial stage of sarcomere formation, the talin, α-actinin, and integrin β1 are clustering periodically at the plasma membrane **(Figure 5)**, which suggests that costameres, providing anchoring sites for sarcomeres at the membrane, are pioneers for the myofibril assembly *in vivo*[25].

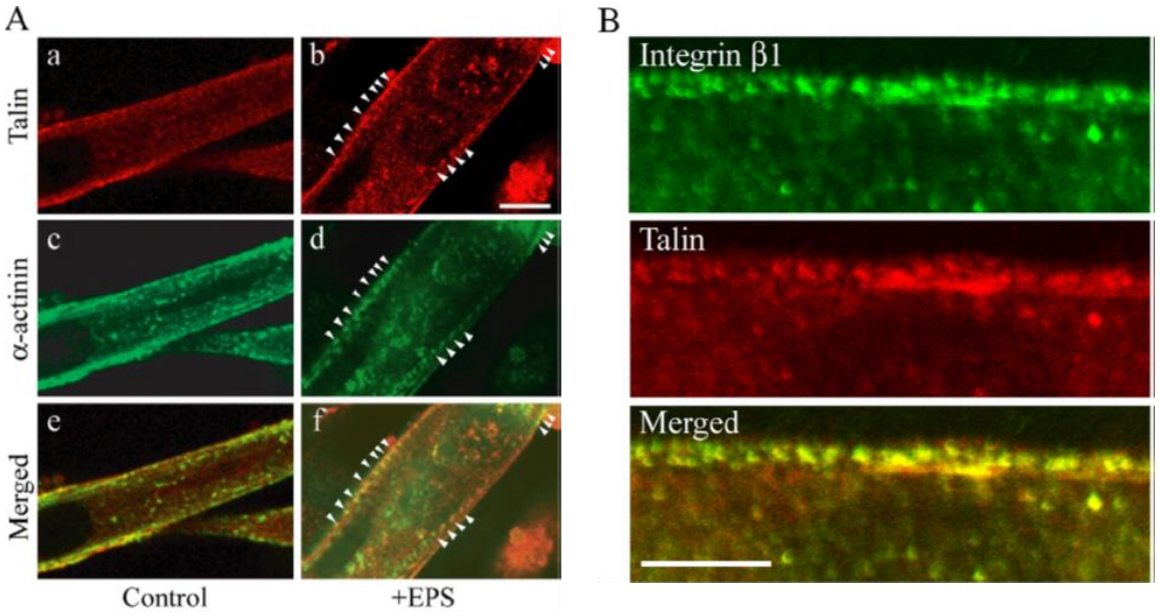


**Figure 5** Immunofluorescent micrographs in Makoto Kanzaki' work. A, talin (red) co-localizing with α-actinin (green) aggregating beneath membrane of differentiated cell showed striated pattern. Scale bar, 5 μm. B, immunofluorescent staining showed integrin β1 (green) and talin (red) clustered at the plasma membrane of myotubes after EPS for 2 hours. Scale bar, 10 μm[25].

Though sharing similar functions and components, the dynamic of costameres and focal adhesion turnovers have rarely been studied connectedly. Protocostameres are the sites where Z-bodies are recruited for initializing the myofibril assembly[16,26]. However, the differences between protocostameres and focal adhesions in striated muscle cells are materially limited. Thus, it is logical to conclude that protocostameres are the intermediates between focal adhesions and costameres during the process of sarcomere assembly, which is important for investigating the dynamic relationships between focal adhesions and costameres.

### 1.1.4. Human induced pluripotent stem cell-derived cardiomyocytes

In the studies of myocardial mechanobiology and regenerative medicine of myocardium, one of the challenges is the cell resource. The freshly isolated human CMs used to be employed in the experiments. However, they are plagued by the shortcoming of the insufficient donated

explants. To address the availability of human CMs, then the animal cell lines were then extensively utilized in drug tests, nevertheless, they are also limited by the inaccuracy crediting to the inherited differences comparing to human. The human-induced pluripotent stem cell-derived cardiomyocytes (hiPSC-CMs) address most of the listed challenges with the maturity of differentiation and maintaining methods[27–29]. However, researchers are still struggling with the immaturities of hiPSC-CMs manifesting as the unaligned morphology, disorganized sarcomeres, and contractions[30–32]. For the seeking of the mature hiPSC-CMs *in vitro*, researchers have created extensive methods to mimic the natural microenvironments and physical/chemical signals to stimulate hiPSC-CMs. A common approach is to optimize the topography of ECM.

## 1.2. Topographical Clue of Extracellular Matrix and Cell-Matrix Interaction

### 1.2.1. Extracellular Matrix

The extracellular matrix (ECM) is a three-dimensional non-cellular structure that provides physical support and biochemical guidance to cells. In general, proteoglycans and fibrous proteins (including collagens, laminin, elastin, and fibronectin) are two main sets of proteins that make up the ECM[33,34] **(Figure 6)**. However, ECM existing in different tissues has a different composition, which suggests that their properties are unique. In healthy cardiac tissue, the collagen I is prevalent, while, in injured myocardium, collagen III is predominant, for instance[35]. By applying the decellularization of natural tissues, people gained the ECM of different organs. Hideaki Fujita's group seeded embryonic stem (ES) cells in liver ECM and cardiac ECM from mouse tissues. The results showed ES cells on heart ECM expressed more cMHC and cTnl in both transcription level and translation level after 3-weeks of cardiac differentiation, which indicated that the heart ECM induced the cardiomyocyte differentiation

of ES cells[36]. With cells linked by focal adhesin, activities of ECM are related to cell differentiation, cell proliferation and cell migration. In mammal hearts, ECM is produced by fibroblast (a large population of non-muscular cells in the heart) and plays as the anchor for cardiomyocytes[37]. Conducted by focal adhesions, the ECM provides mechanical cues to cells, and the cells sense the signals and respond in turn, which forms the interactions between cells and ECM. For instance, ECM with different stiffnesses would affect the force generation of cardiomyocytes while RhoA/ROCK pathway is involved in assisting cardiomyocytes to adapt a wider variation of ECM stiffnesses[38].

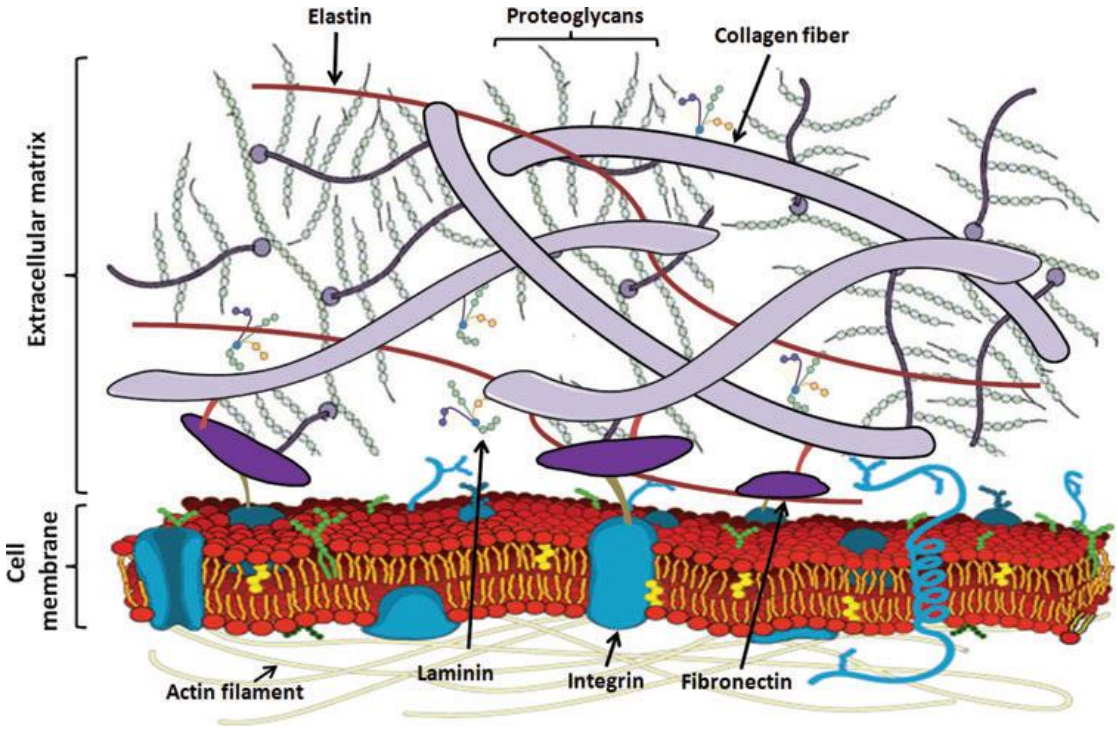


**Figure 6** Components of ECM proteins[39].

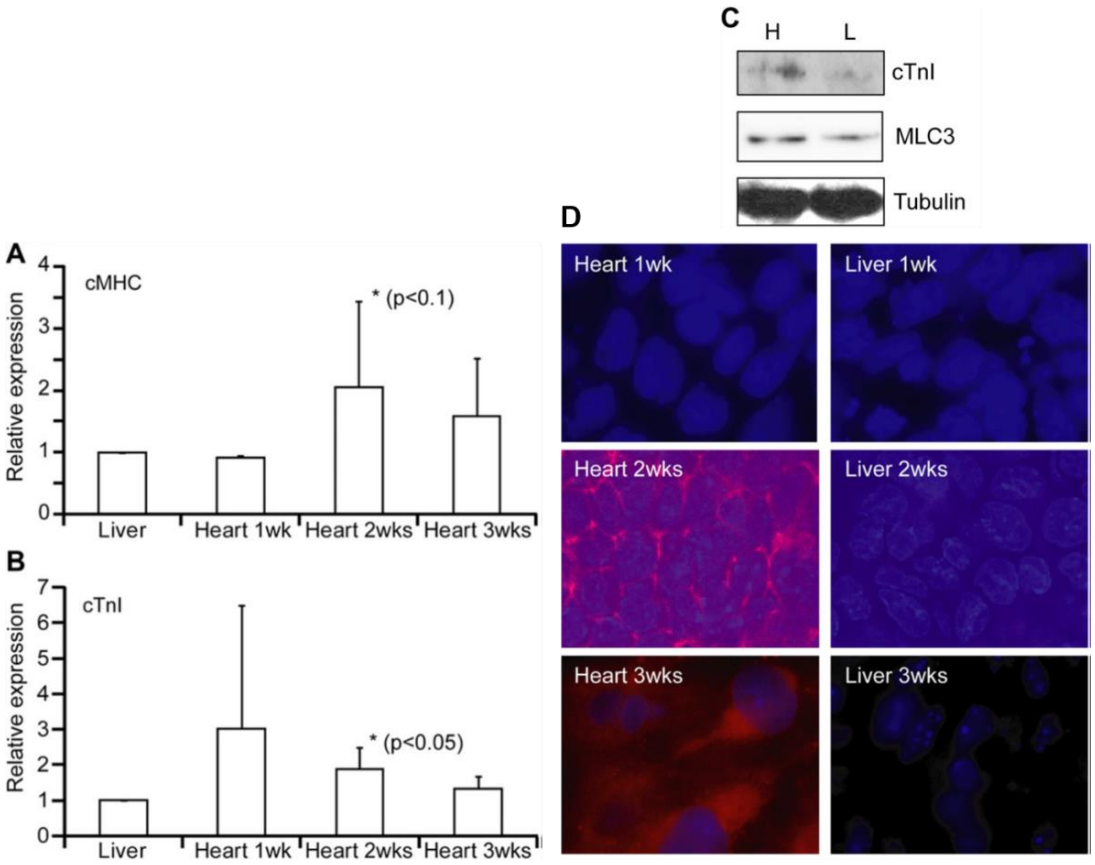


**Figure 7** Results of ES cells cardiac differentiation.

### 1.2.2. Topographical cues to cells

Given the critical role ECM plays in cell development, biophysical cues from different topography of substrates have been created and used by researchers to positively affect cells. Polydimethylsiloxane (PDMS), a non-toxic biological polymer, has been widely used for creating the surface pattern in substrate polymerizations. In 2013, Cesare M. Terracciano utilized photolithography for microtexturing the PDMS substrate with microgrooves (**Figure 8 E**). The microgrooved PDMS was coated with fibronectin for cardiomyocyte attachment. Cardiomyocytes were then seeded on the structured (microgroove patterned) and non-structured (flat) substrates for comparison. The results showed the alignment of cardiomyocytes on the microgrooved surfaces had been promoted. The $Ca^{2+}$ cycle in the microgrooved group was shortened significantly compared with the flat group, which suggested the microgroove pattern may help the maturation of induced pluripotency stem

cell-derived cardiomyocytes (hiPSC-CM) (**Figure 8 A-D**)[40]. In 2016, Song Li et al. used the above described method to create substrates with microgrooves and investigated the effect of biophysical cues to cardiomyocyte reprogramming. The data indicated that the expression of cardiomyocytes genes has been enhanced after 2 days culturing on the microgrooved substrates, and the yield of the reprogrammed striated cell has been improved after 10 days, which indicated the microgrooves can accelerate the reprogramming process via enhancing gene expression and sarcomere structures[41]. Wei-Bor Tsai fabricated nanoscale groove structures on substrate surface to investigate the cell elongation, alignment, and focal adhesion alterations on nanoscale groove substrate (**Figure 9**). PDMS was used to complement the nanotextured silicon wafer. 5% (w/v) polystyrene (PS) in toluene and 20% (w/v) polyurethane (PU) in dimethylformamide were covered with carved PDMS to form nanogrooved PU and PS surfaces. After 2 days culturing, the focal adhesion complexes on nanogrooved surfaces were parallel to grooves and less isotropic than on flat surfaces[42].

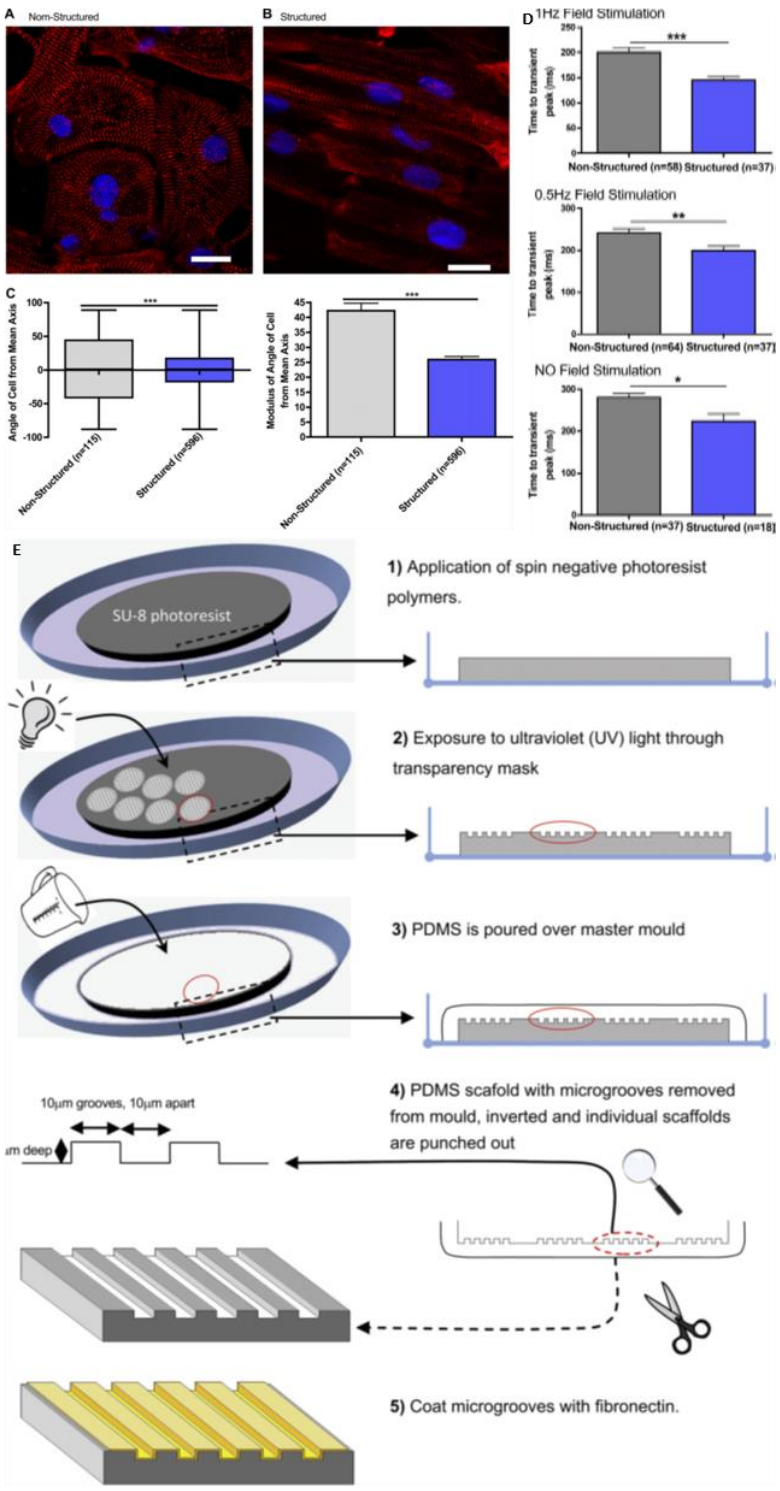


**Figure 8** Microgrooved pattern utilized in cardiac research. A-D, results of iPSC-CMs cultured on microgrooved substrate and flat substrate. A, immunofluorescence of iPSC on unstructured PDMS. B, microgrooved PDMS, red is sarcomeric α-acin, blue is DAPI, scale bar, 20 μm. C, cell alignment of iPSC-CM on structured and unstructured substrates. D, time to peak of $Ca^{2+}$ transient. E, flow chart of microgroove substrate fabrication[40].

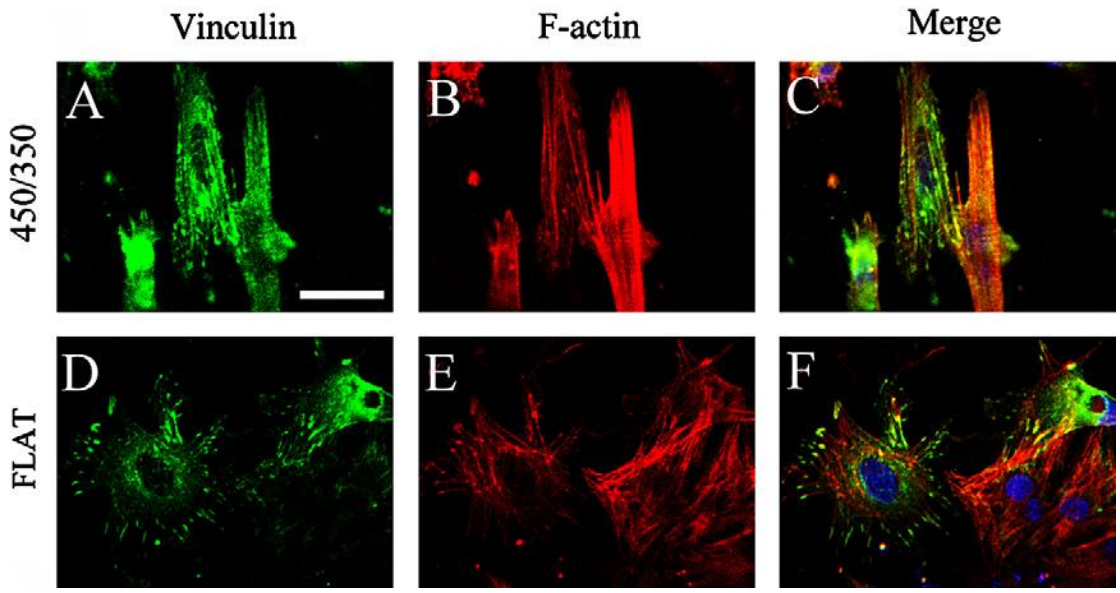


**Figure 9** Focal adhesions staining using vinculin as mark. Immunofluorescent image showed the vinculin formation is align with the direction of groove[42].

Another application of photolithography for patterned substrate surfaces is the nanopillar topography. Normally, a PDMS or polyurethane acrylate (PUA) plate with a nanopillar pattern is used as the mold. The mold then may contact conformally with a glass whose surface has been dropped with poly (ethylene glycol)-dimethacrylate (PEG-DMA) or other biomaterials with the capability of serving as substrates. The molded sample will be cured under UV light for crosslinking and then be peeled off the mold (**Figure 10 A**) when the substrate with nanopillar topography is ready (**Figure 10 B**)[43].

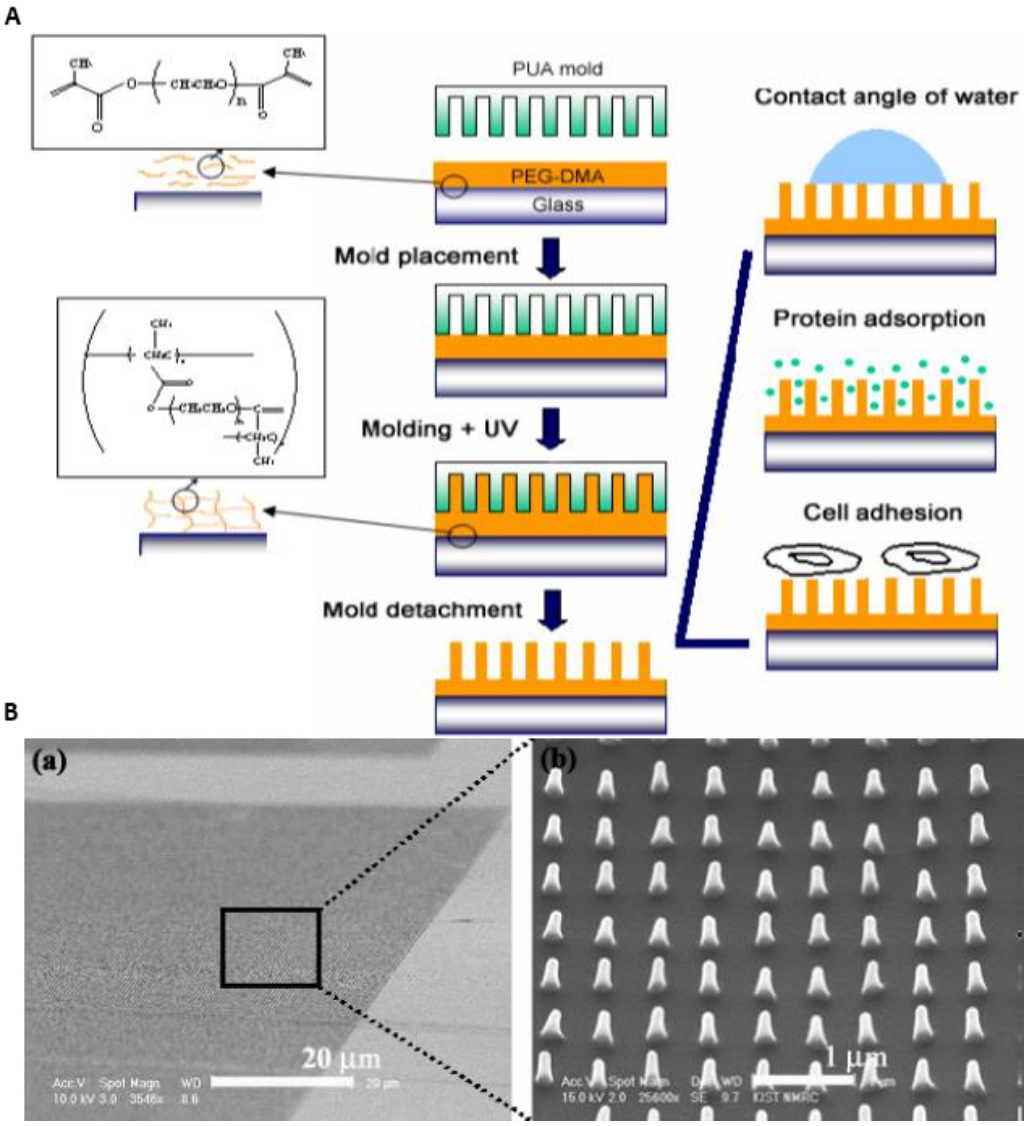


**Figure 10** Nanopillar PEG-DMA substrate. A, schematic illustrating of PEG-DMA nanopillar topographic substrate fabrication. B, SEM image of nanopillar PEG substrate. (a) the large area view showing patterned region (dark area) and non-patterned region (light area). (b) the magnified view of the nanopillars of the box in (a)[43].

Peilin Chen used this pattern with different pillar heights to investigate the movements and focal adhesions of cells. The results showed that with pillar heights of 800 nm and 1200 nm, the focal adhesions of ovary cells formed directionally aligned with the vertical and horizontal direction of pillar arrangement (**Figure 11**)[44].

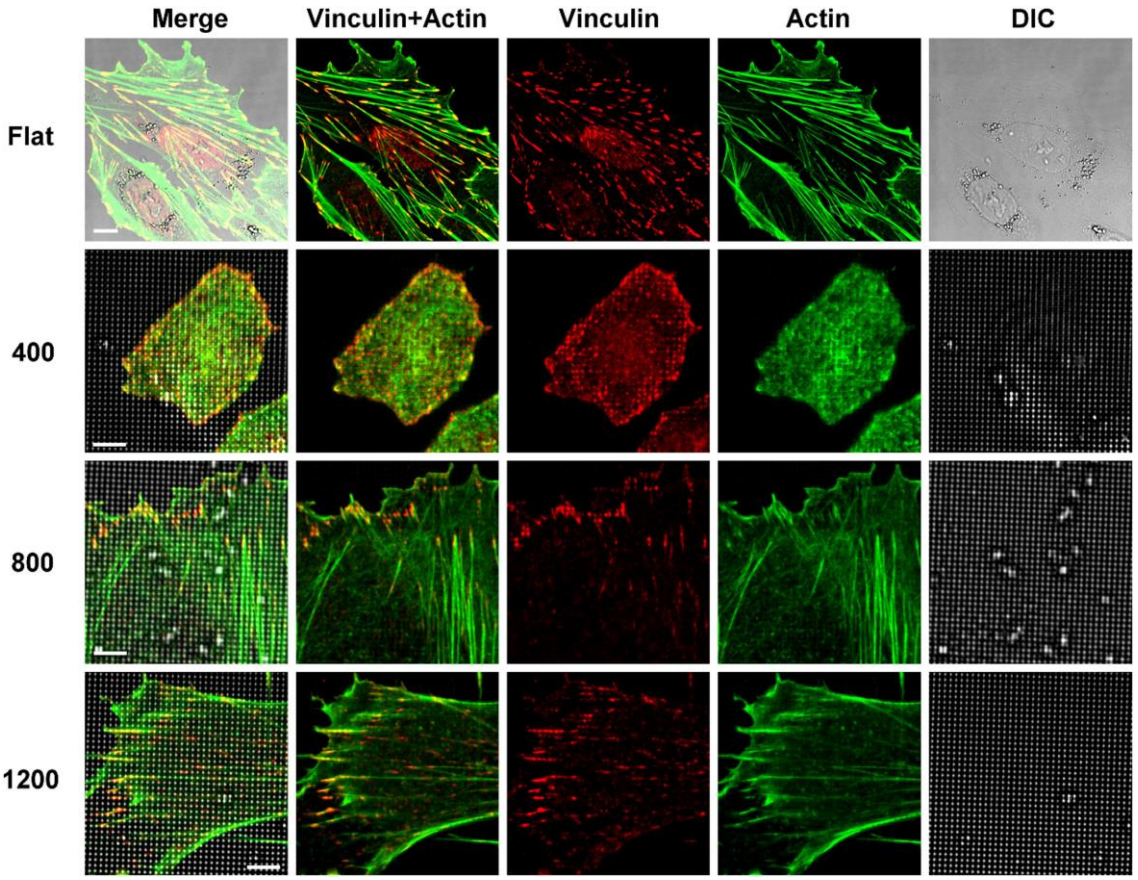


**Figure 11** Immunofluorescent images of cells on substrates with different height of nanopillars[44].

Based on the nanopillar surface, Dong-Weon Lee's group added the microgroove pattern on the tip of the pillar. The process flow is shown as **Figure 12 A**. The results indicated that the cardiomyocyte alignment and the cardiomyocyte beating on pillars with grooves were isotropic along with groove direction, while were anisotropic on pillars without grooves. The contraction force of cardiomyocytes is significantly higher on pillars with grooves[45].

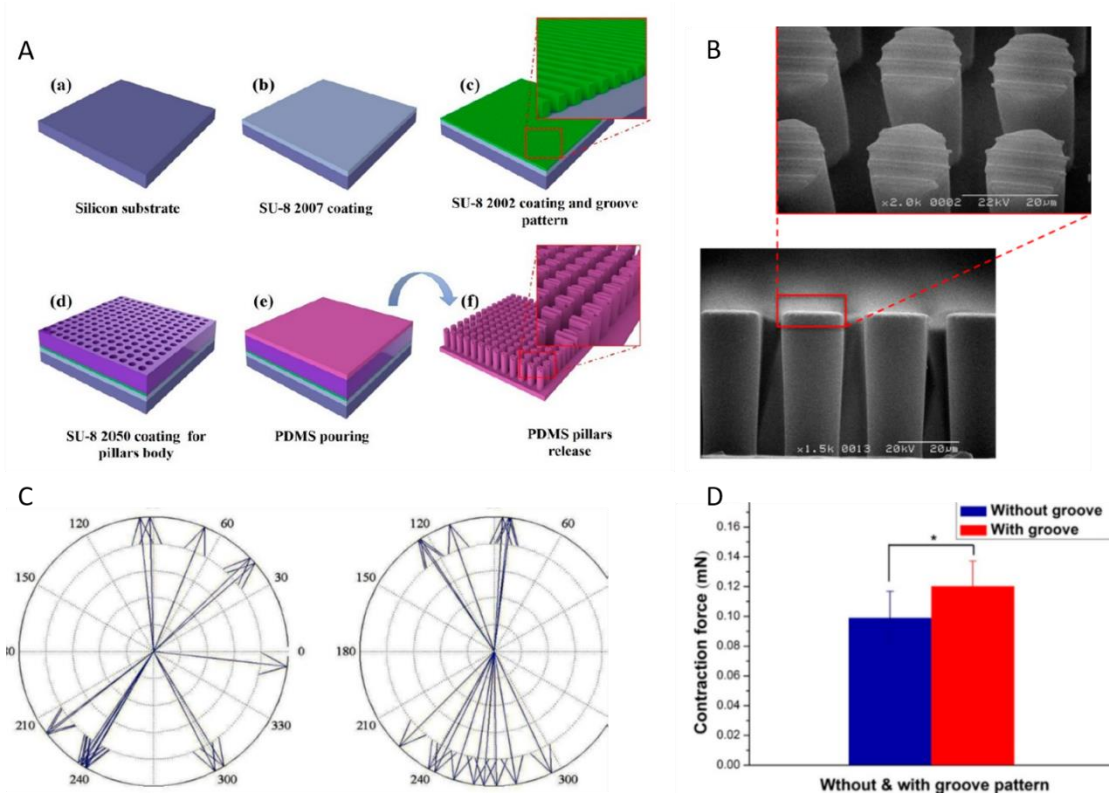


**Figure 12** Nanopatterns used in cardiac research. A flow of PDMS pillar arrays with grooves on the top; B, SEM image of cross-sectional view of grooves pattern on pillars; C, vector analysis of cardiomyocytes beating; D, contraction force on pillar arrays with or without grooves.

Except for nanopillars and nanogrooves, the employment of electrospinning enables a cost-effective and simple fabrication of a nanofiber scaffold, which augments the comprehension of the role that ECM plays on affecting tissue engineering application. Seeram Ramakrishna fabricated nanofiber substrates by polycaprolactone (PCL) and polycaprolactone/gelatin (PG). The substrates were designed as random PG/PCL composite fibrous substrates and aligned PG/PCL fibrous substrates (**Figure 13**). The cell experiment showed that aligned PG nanofibrous scaffolds enhanced cell attachment and promoted cell alignment along fibrous direction[46]. Another application of a nanofibrous substrate from the same group was using poly (D, L-lactide-co-glycolide) (PLGA) and poly (D, L-lactide-co-glycolide)/collagen (PLGA/Col) as the substrate material to investigate how fibrous substrate affects embryonic stem cell differentiation. The result showed PLGA/Col whose fiber diameter is smaller

provided better mechanical and chemical support enhancing ESCs growth and differentiation to cardiomyocytes[47].

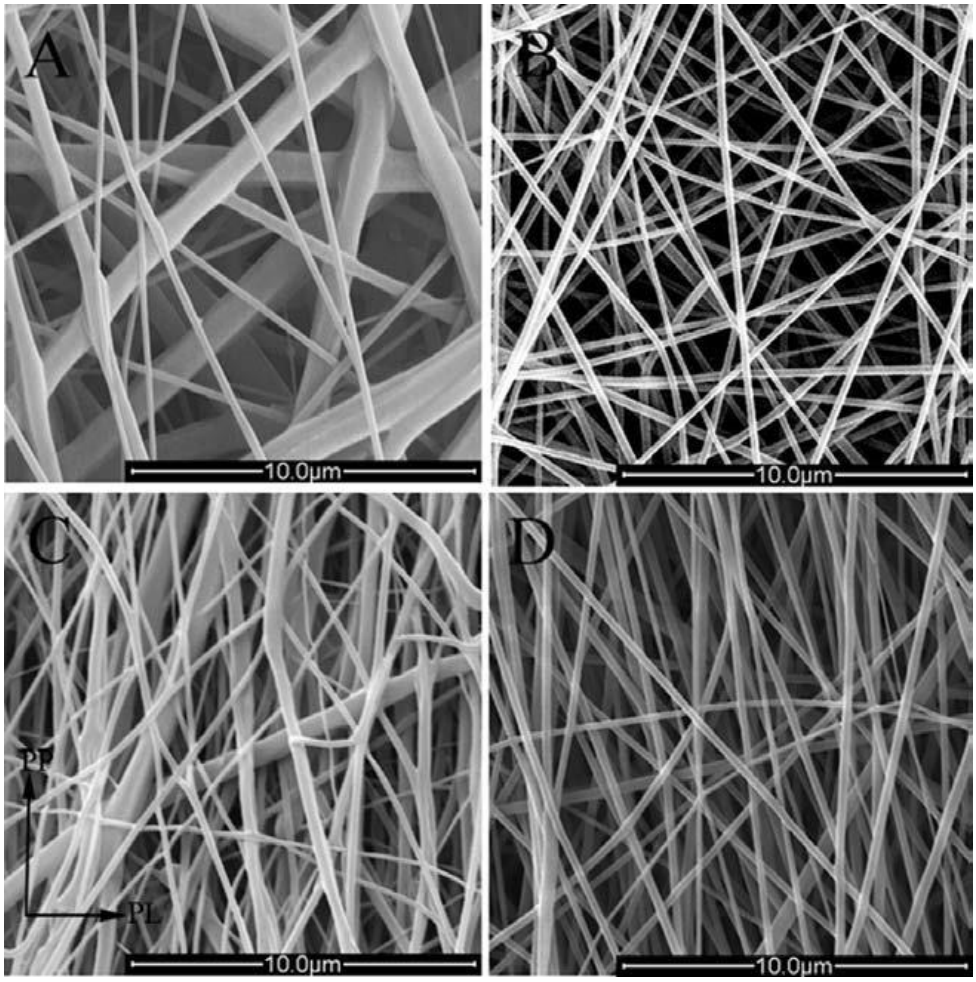


**Figure 13** SEM image of nanofibrous substrate. A, random PCL; B, random PG; C, aligned PCL; D, aligned PG[46].

In 2009, Michelle Khine's group fabricated nanowrinkled texture with different scales. A metallic layer using gold-palladium was deposited on the PS prestressed sheet. Then the PS sheet was induced to shrink thermally, during this process, the metal layer on the PS sheet was brought to form anisotropic or isotropic wrinkles, depending on the direction of shrink. The wrinkled metal layer was used as the lithography mold to generate the PDMS substrate with a complimentary wrinkle surface (**Figure 14**)[48].

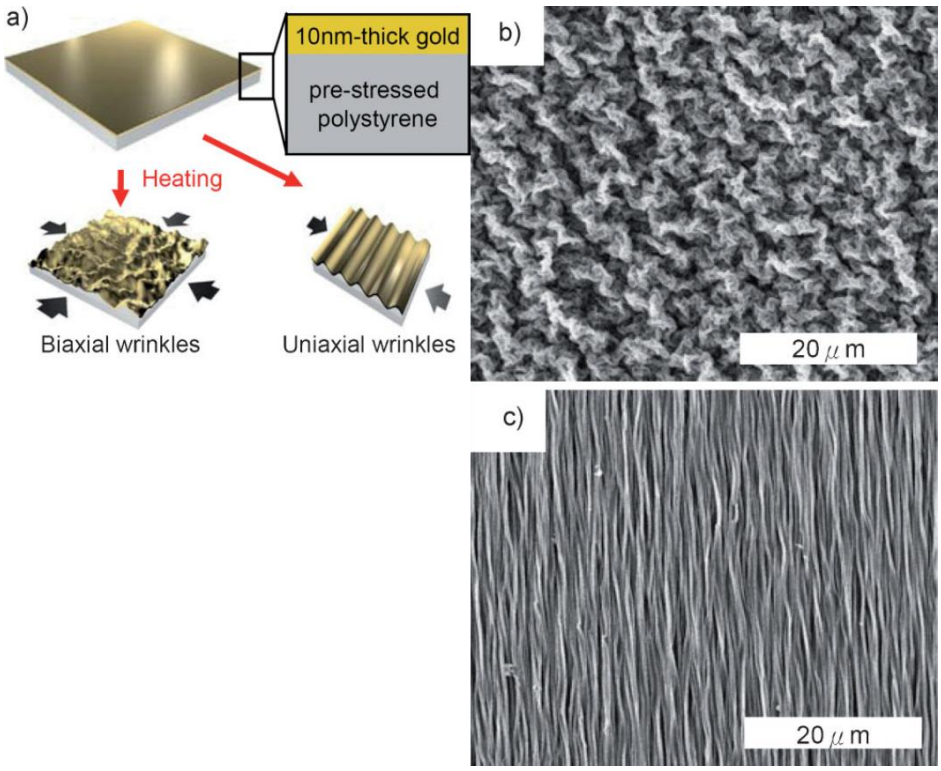


**Figure 14** Formation of wrinkle surface and SEM images. Shrinking of PG under thermal treatment brings gold layer (a) forming biaxial wrinkles (b) and uniaxial wrinkles (c)[48].

Employing the above protocol, Dr. McCloskey seeded cardiomyocytes and human embryonic stem cell-derived cardiomyocytes (hESC-CMs) on nanowrinkled substrates. The results showed that the cardiomyocytes and hESC-CMs had better alignment and actin orientation on the nanowrinkled surfaces (**Figure 15**)[49].

In 2013, Franceso Greco modified Khine's protocol and fabricated the PS substrate and generated the wrinkle surface using poly (3,4-ethylenedioxythiophene): poly (styrene sulfonate) (PEDOT: PSS) coating. The thermo-retractable PS sheet was treated by air plasma. Then the PEDOT: PSS was spin-coated on the surface of a polystyrene sheet. As the PS substrate with PEDOT: PSS coating was under thermal treatment, the wrinkle formed, and the direction of wrinkle aligned with the shrink direction, perpendicular to clamps (**Figure 16**). The C2C12 cells were seeded on both a nanowrinkled surface and a flat surface. The

results indicated that the wrinkled structures were able to transfer a preferential guidance to the fibroblasts, which further directed C2C12 cells and enhanced their alignment along the wrinkle direction[50].

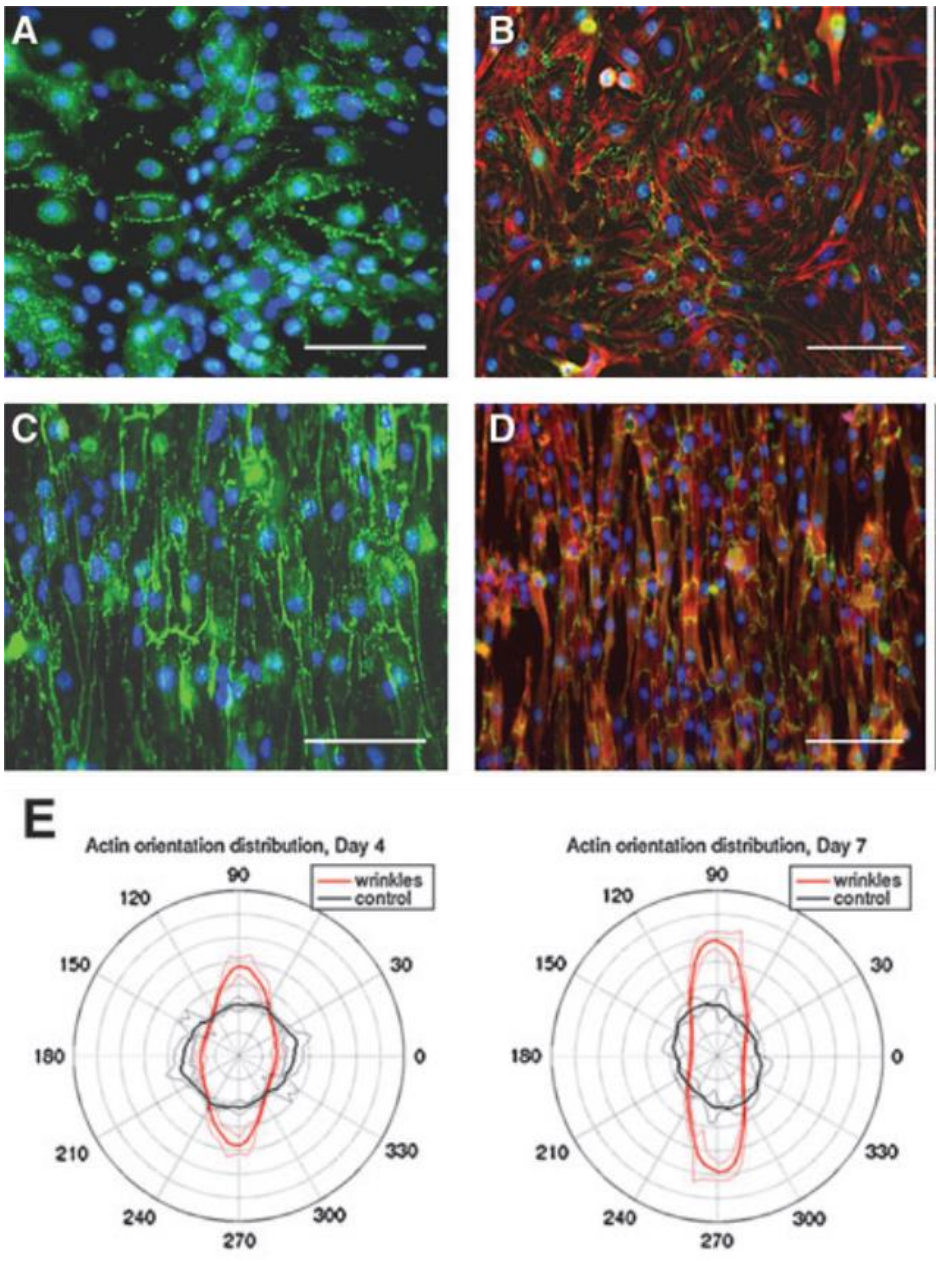


**Figure 15** Fluorescent images of cardiac tissue on flat surface (A, B) and nanowrinkled surface (C, D). Red, actin; Green, N-Cadherin; Blue, nuclear staining DAPI, scale bars = 100 μm. E, anisotropy analysis of actin orientation on wrinkled surface (red line) and flat surface (black line) after 7 days culturing[49].

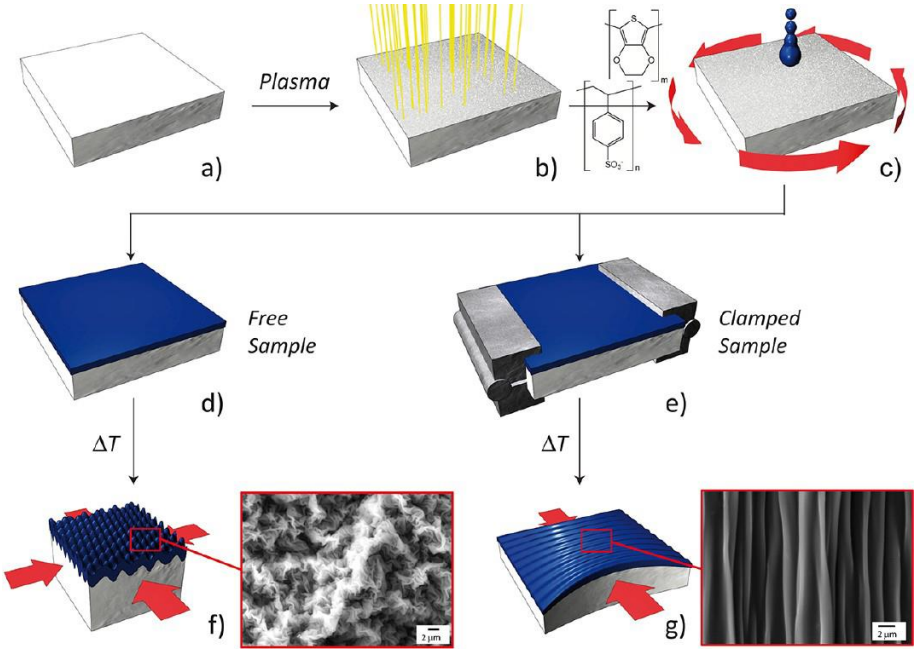


**Figure 16** Sketch of wrinkled surface substrate formation. Red arrows in (f) and (g) showed wrinkle directions, red boxes in (f) and (g) showed SEM image of nanowrinkle topography[50].

In a 2018 study, Morteza Mahmoudi and their colleagues used a subtle method to create a multiscale topographic substrate. The mature cardiomyocytes were cultured and fixed on a flat surface to form the mold. PDMS was used as complementary and formed the "cell-imprinted substrate"; a PDMS covering on the top of a semi-cylinder-patterned surface formed the substrate with cell scale sinks is defined as a "micropatterned substrate" (**Figure 17**); the induced cardiomyocytes cultured on a micropatterned substrate fixed to form the mold on which the PDMS is dropped to generate the substrates is called a "multiscale-imprinted substrate". iPSCs were then cultured on these three different substrates and were induced to differentiated into cardiomyocytes. The results indicated that the multiscale imprinted substrates were able to accelerate the differentiation process most effectively while the micropatterned substrates were excellent at maturing the induced cardiomyocytes[51].

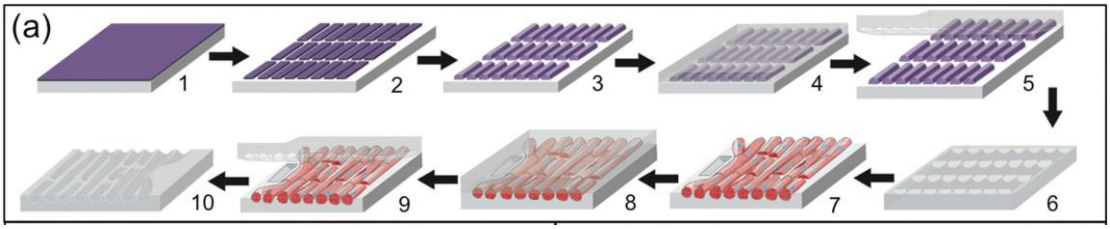


**Figure 17** Schematic representation of microfabrication and cell-imprinting process. Micropatterned surface is shown as (6), the red columns in (7), (8), (9) stand for cardiomyocytes. (10) illustrates the multiscale imprinted substrate[51].

### 1.2.3. Cell response to dynamic substrate

The situation of cell morphologies and cell actions on substrates with multiple topographies has been well studied, and researchers are still creating new platforms to alter the substrate surfaces for mimicking natural ECM. The natural extracellular microenvironment where cells live is highly dynamic, which directs cells temporally and spatially through chemical cues, physical cues, or both. However, how cells respond to the dynamic alterations from ECM has been limitedly understood. Shana O. Kelley used potential responsive surfaces to investigate how the cell adhesions and cell differentiation had been facilitated dynamically under different potentials. The results showed that under 200 mV for 2 hours, the RGD (Arg-Gly-Asp) peptides were exposed and the cell adhesion was strengthened; while shifting the potential from 200 mV to -200 mV for 1 hour, the RGD was concealed and cell attachment was decreased significantly (**Figure 18**)[52]. In addition to the alteration of ligands on a surface, the dynamic alteration of topographic features can also guide cell activities. James H. Henderson's group used a shape memory polymer to demonstrate that a micron-scale grooved surface could recover to flat under thermal treatment. During this dynamic process, the cells seeded on the substrate experienced morphological remodeling from anisotropic (align to groove direction) to isotropical[53].

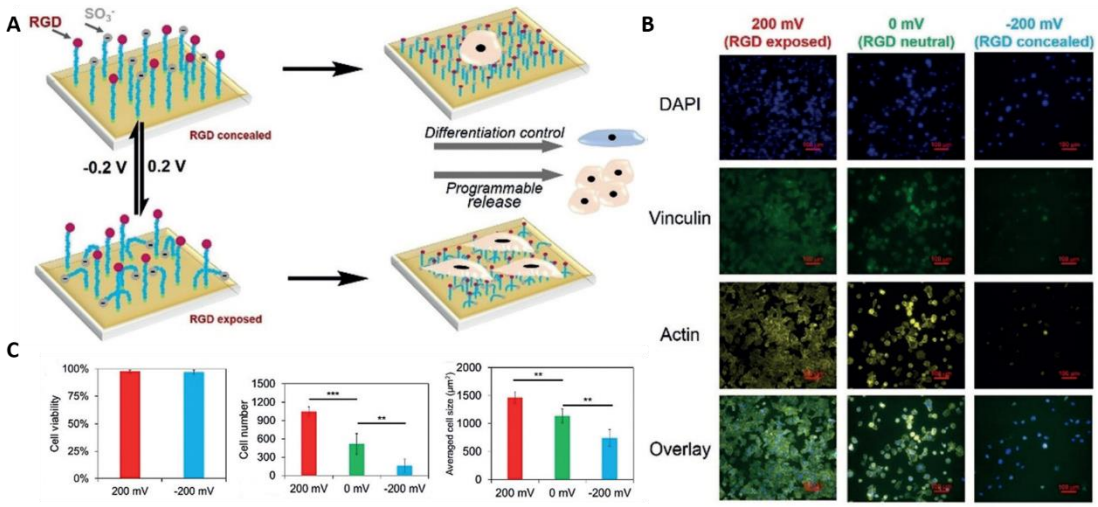


**Figure 18** Potential responsive material in Shana O. Kelley's work. A, sketch shows potential-responsive RGD peptide regulating cell adhesion. B, Fluorescent images of cells on substrates under different potentials[52].

Kenneth B. Margulies' group utilized a magnetic field to change the stiffness of the substrates and investigated the dynamics of cardiomyocyte responses against different stiffness substrates. The stiffness of substrate was negatively related to the distance between the substrate and the magnet. The results indicated that the cardiomyocyte spreading, percent of myofibroblast activation, and sarcomere organization were related to the stiffness of the substrate. When the stiffness decreased, the sarcomeres became disorganized (**Figure 19**)[54].

Jennifer L. Young and Adam J. Engler fabricated hydrogels using thiolated-hyaluronic acid (HA) whose elastic module increases time-dependently. The cardiomyocytes were cultured on it to see how the changing stiffness from hydrogel guided the cell activities. The alignment of cardiomyocytes was enhanced and the late cardiac marker expressions were augmented, which indicated a dynamic HA hydrogel substrate enhanced the maturation of cardiac muscle[55].

Deok-Ho Kim's group, using shape memory polymer, fabricated a substrate having the

capability of changing nanotopographic cues of the surface. The orientation of nanogrooves on the surface could practice an orthogonal orientation transition under 37 ℃ treatment. Cardiomyocytes on the permanent static grooved substrates served as a control group to examine how cardiomyocytes respond to the dynamic nanotopographic clue. The results indicated that the contraction orientation, as well as nuclei alignment, were in line with the groove direction before the transition and were more random after transition (**Figure 20**)[56]. Nevertheless, most studies about dynamic substrate focus on the comparison of cells in different microenvironments, which can be seen as end-to-end researches. The real-time situation of cells during substrate change is still poorly understood.

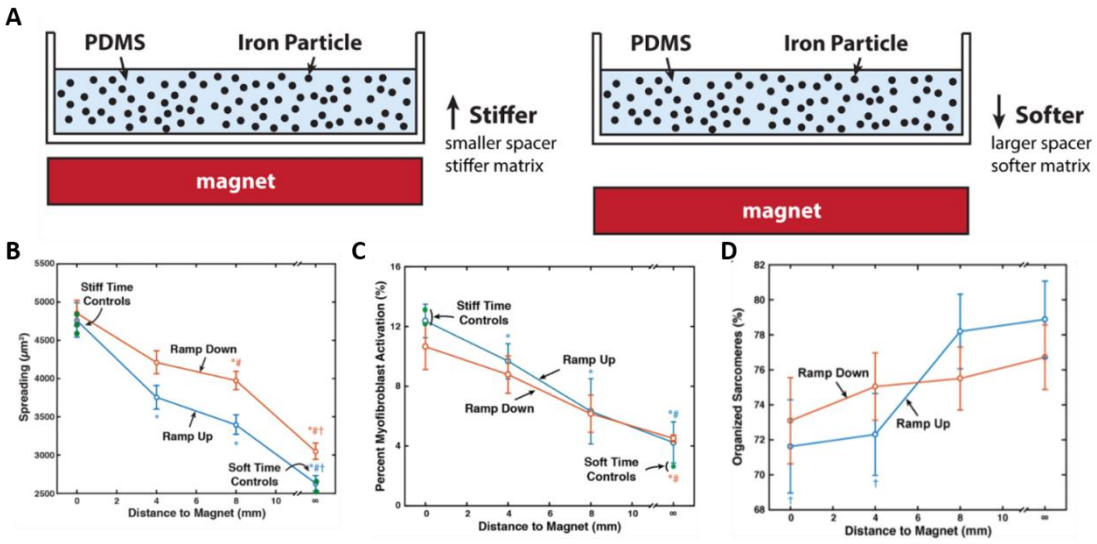


**Figure 19** Magnet responsive materials in cardiac research. Dynamic control of substrate stiffness, the magnetic field was tuned by the distance between magnet and substrate. B-D, results of cell experiment with spreading (B), percent myofibroblast activation (C) and sarcomere organization (D)[54].

### 1.2.4. Applications of active biomaterials for focal adhesion research

Shape memory polymers are materials polymerized by a single or multiple monomers and have the ability to recover the original shape after deformation under certain stimulations

such as light activation[57], water or solvent driven[58], thermal activation[59], etc. The assembly of focal adhesions has been proved to be affected by texture properties of a substrate[60,55,56] , but when the substrate topographic clue changed, the focal adhesion complexes have disrupted during the substrate dynamic (**Figure 20 C**)[56]. Takao Aoyagi's group utilized a temperature-responsive PCL film to investigate the cell morphological change during substrate dynamic change. During the crystal-amorphous transition of PCL, the surface changed from rough to flat, during this process, the cells shrank into balls and further detached[61].

Paolo A. Netti's team seeded NIH-3T3 fibroblasts on a polymer with a light-responsive film. The vinculin was stained to illustrate the behavior of the focal adhesions. The results showed the focal adhesion orientations changed dramatically after 24 hours' seeding on substrates with flat surfaces, wrinkled surfaces, and wrinkled to erased surfaces. The directions of focal adhesions were anisotropic on the flat surfaces first, and in line with the wrinkle direction then, and finally became anisotropic again on erased surfaces[62]. However, in the study, the results were collected after seeding on each status of substrate for 24 hours, which means the cell responses caused by dynamic substrate have completed and the dynamic responses of cells are still missing.

The shape memory polymers having the merit of changing topography gradually with living cells provide an opportunity to study the dynamics of cells responding to substrate changes. Focal adhesions are the large molecular complexes that anchor cells to the extracellular matrix (ECM), which is involved in cell spreading, migration, and proliferation. In our previous work, the study of cardiomyocyte morphological changes and myofibril remodeling, responding to dynamic nano-topographic substrate, have been documented. The results showed focal adhesions experienced disassembly and reassembly in the first 12 hours.

However, when the disassembly and reassembly happened exactly and how the progress was are still unknown. To investigate the details of focal adhesion remodeling, paxillin, vinculin and zyxin were chosen as markers to stand for three layers of focal adhesive complex from the ECM side to the cell plasma side. The length, fluorescence signal intensities, densities of stained structures were examined for tracking the sequential alteration of focal adhesion complex.

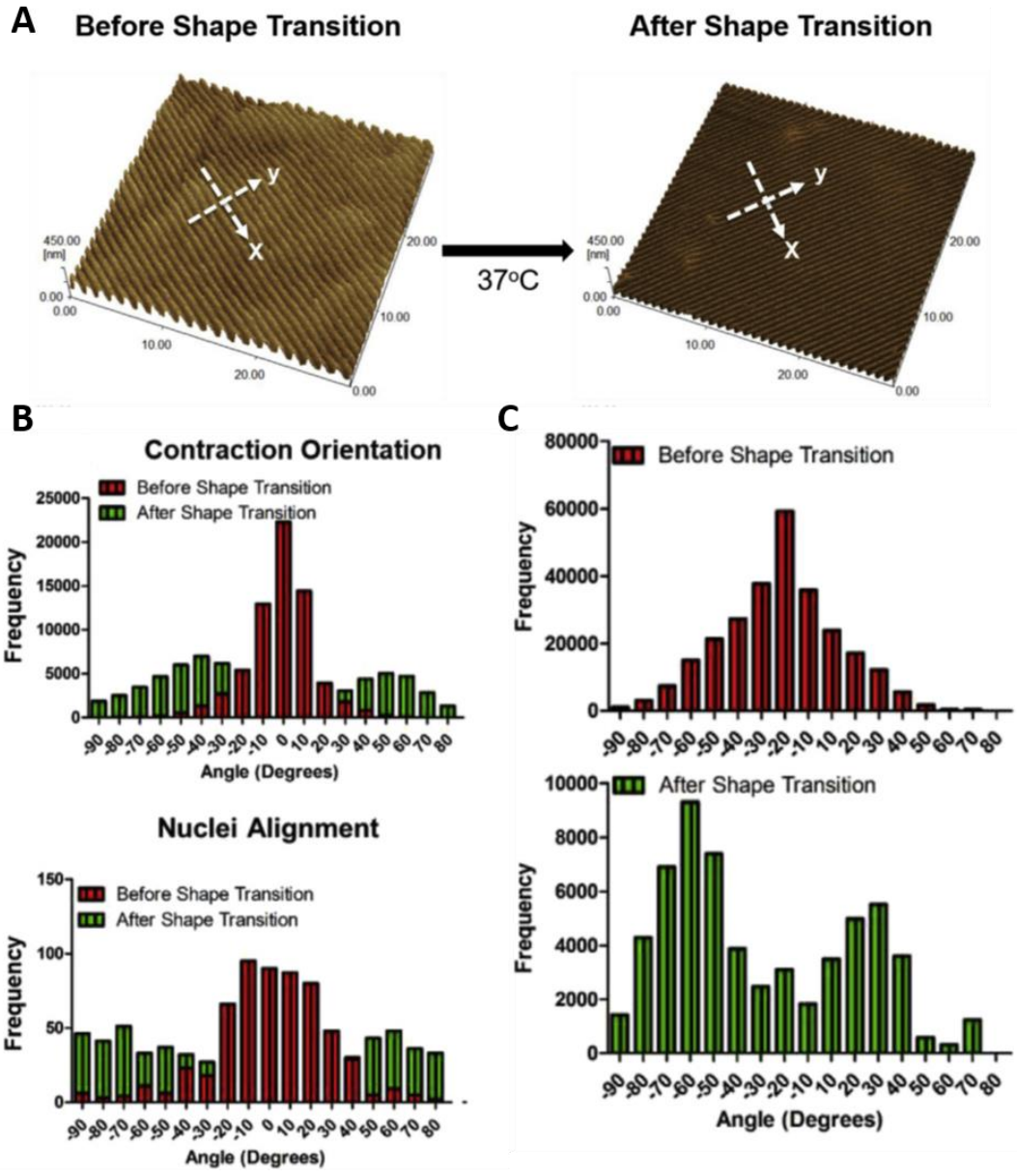


**Figure 20** Utilization of SMP in focal adhesion study. A, AFM images of topographies before shape transition and after shape transition. B, contraction orientation and nuclei

alignment of cardiomyocytes on substrate before and after shape transition. C, vinculin orientation distribution before and after shape transition[56].

# 2. Materials and Methods

## 2.1. Overall

To investigate the responses of cardiomyocytes to the surface change, the shape memory polymer was used to create a dynamic topography. Generally, the whole process can be described as the preparation of cells and polymers, dynamic substrate formation, and data collection and analysis. For the preparation of polymers, the Tert-Butyl Acrylate (tBA) was employed as the main monomer in fabrication for giving the property of recovery shape at low temperature, which fulfills the prerequisite of cell survival. The polymer processing includes polymer fabrication, stretching, coating for wrinkle surface, sterilization, and coating for cell attachment. Then, cardiomyocytes were seeded onto the polymer surface under the temperature ensuring polymer non-deformation as well as cell survival. The polymers with cells were switched to a higher temperature for triggering the formation of wrinkle surface. The data was collected at different time points after polymer starting recovery for analyzing the cardiomyocyte responses.

## 2.2. Shape Memory Polymer Fabrication and Processing

### 2.2.1. Polymer Fabrication

The shape memory polymer has four components including the monomers Tert-Butyl Acrylate (TBA) and Butyl Acrylate (BA), and crosslinker Tetraethylene glycol dimethacrylate (TEG DMA), and photoinitiator 2,2-dimethoxy-2-phenyl acetophenone (DMPA). TBA, the main material giving polymer the property of shape recovery weighs 95

present of monomer solution while BA weighs 5 present. DMPA weighs 1 present of total weight of TBA and BA. The volume of TEG DMA is the same as the volume of BA. The volume of TBA and BA can be calculated as followed:

TBA:

$$\frac{(\text{Mass of DMPA in grams}) * (\text{weight percent of TBA})}{(\text{density of TBA})}$$

BA:

$$\frac{(\text{Mass of DMPA in grams}) * (\text{weight percent of BA})}{(\text{density of BA})}$$

In the formulas, the density of TBA is 0.875 g/ml while the density of BA is 0.894 g/ml. The mold used to contain the mixed polymer solution includes two glass slides and one Teflon spacer between two glass slides, which form a sandwich-like structure. The inner side of each glass slide needs to be coated with Rain-X to make it hydrophobic, which avoids crosslinked polymer adhering to the glass slides. The binder clips were employed to clamp the periphery of glass-Teflon-glass structure to avoid leakage.

As added the mixed solution into mold, the mold was moved into an ultraviolet (UV) box for crosslinking. After 1-hour crosslinking, the solid polymer was removed from mold and immersed into 50% methanol solution (methanol: deionized (DI) water, 1:1 v/v). Methanol solution with polymer was placed to a shaker for six hours to extract the TBA and BA monomer from crosslinked polymer. The washed polymer was placed into a chemical hood for drying over six hours and then further drying by putting into a vacuumed oven for six hours under room temperature. The twice-dried polymer was ready to use.

### 2.2.2. Polymer Stretching

Fabricated polymers need to be cut into small pieces with size 2.3 cm × 0.5 cm, rectangle shape. The stretching of cut polymer was carried out manually. One piece of polymer was fixed with 2 clips of a stretcher, which was tightened by 4 screws applied ~3N forces. After setting up, the stretcher together with polymer were placed in a 70 ℃-preheated oven for 10 minutes. When the polymer became ductile and soft, slowly stretched the polymer by rotating the knob of the stretcher to 140% of its original length. The stretched polymer and stretcher were taken out of the oven and cooled down to room temperature. Then the polymer is ready for the next step processing.

### 2.2.3. Polyelectrolyte Multilayers (PEM) Film Deposition

The wrinkle pattern on SMP surface comes from the PEM layer that can be brought by the shrink of SMP during the recovery and forms the wrinkle. The PEM film consists of a layer of PEI, 20 layers of PSS, 20 layers of PAH coating, and 80 times of water rinse. The stretched polymer was fixed by double-sided tape in the center of a spin coater. Firstly, the PEI solution was dropped onto the top of polymer by pipette. The surface of polymer needed to be fully covered by PEI liquid drop and then spin-coated for 12 seconds at 3000 RPM. The next coming was 20-bilayers coating. Each bilayer included one layer of PSS coating, two times of DI water rinses, one layer of PAH coating, and two other times of water rinses. After every time liquid coating including PAH, PSS, and DI water, the spin coating was 12 seconds at 3000 RPM.

### 2.2.4. Geltrex Coating

After the PEM coating, the polymer needs to be cut into smaller pieces that are accord with the size of a single well of 48-well plate. The cut polymers were then sterilized under UV in the hood for 1 hour (30 minutes for one side, double sides). The sterilized polymers were moved into 48-well plate with Geltrex solution in the well. The polymers with 48-well plate was then placed under room temperature overnight, which is to help the attachment of cardiomyocyte. The protocol of polymer fabrication and processing is shown in **Figure 21**.

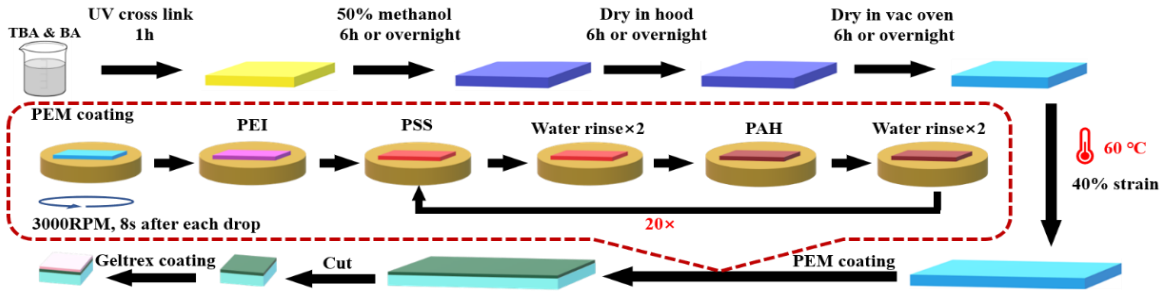


**Figure 21** Schematic illustration of SMP fabrication and PEM coating.

## 2.3. Cell Preparation

### 2.3.1. Cell Culture

The cardiomyocytes derived from human induced pluripotent stem cells. hiPSC-CMs are maintained using RPMI media with B-27 supplement (RPMI-B27) in 6-well plates in the incubator with 5% $CO_2$ under 37 ℃. The media needs to be refreshed every 2 days.

### 2.3.2. Cell Seeding

After aspirating the medium in well, the hiPSC-CMs were washed using PBS to rinse the

remaining medium. Then 0.025% trypsin was added into well for 5 to 12 minutes under 37 ℃ for cell detachment. 37 ℃ preheated EB 20 was then added into the well to end the digestion of trypsin. The cell suspension was centrifuged at 800 RPM for 5 minutes. After centrifuge, getting rid of the supernatant and re-suspending cells with RPMI-B27 media. RPMI-B27 for re-suspending cannot be warmed up with a temperature higher than 30 ℃ to avoid polymer recovery. Based on the optimization, 30,000 hiPSC-CMs were seeded into one well (48 wells plate) containing one piece of geltrax-coated SMP-PEM substrate. Hemocytometer was utilized to count cell for guaranteeing the seeding number. The volume of the medium for each well was 500 μl. Y-27632, a ROCK inhibitor was added into suspension to make a 10 nM concentration solution. After cell seeding, the 48 well plate was incubated in a 30 ℃ incubator with 5% $CO_2$. The medium should be refreshed in the next day after cell seeding to get rid of the ROCK inhibitor.

### 2.4 Data Collection

#### 2.4.1 Triggering Wrinkle Formation

Cardiomyocytes on SMP-PEM were allowed to spread for 2 days at 30 ℃. Then, the plate was transported to 37 ℃ to initiate the polymer recovery, as well as wrinkle formation. The hour 0 is defined as the cardiomyocytes at this point. For timeline experiments, one polymer with cardiomyocytes was taken out the plate each 1 hour from hour 0 to hour 6, which gave a total of 7 samples recorded as hour 0, hour 1, hour 2, hour 3, hour 4, hour 5 and hour 6. The polymers taken out were then operated to fix the cardiomyocytes (**Figure 22 A**). For the baseline, the cardiomyocytes were allowed to grow on static flat surface, static wrinkled surface and dynamic wrinkle surface for 36 hours after triggering wrinkle formation, then the samples were taken out for fixation and staining. The flat surface was the polymer recovering

to its original length after stretching, then the 20 bilayers PEM coating were implemented. The static wrinkle surfaces were PEM-coated polymer recovered before cell seeding. The cardiomyocytes were directly seeded on the wrinkled surface (**Figure 22 B**).

### 2.4.2 Cell Fixation and Fluorescent Staining

After taken out, the polymers were washed by PBS for 3-5 times, 4% PFA solution was used to fix the cells. After treating by PFA for 20 minutes, the samples were washed by PBS solution for 3-5 times again. 0.2% triton solution was then added into wells to cover the polymer for 5 minutes. Next, 2% BSA solution was used to replace the triton solution to cover the polymer for 30 minutes. After removing the BSA solution, the primary antibodies of zyxin, vinculin, and paxillin were used to incubate the polymers for 1.5 hours. The working concentration of primary antibodies was 1-4 μg/ml. After primary antibody incubation, washing samples by PBS for 3-5 times, added secondary antibodies to stain the proteins labeled with primary antibodies. Also, the conjugated anti-actin antibody was used to stain thin filaments in sarcomere and skeletal actin fibers. The secondary antibody incubation needed 1.5 hours as well. Upon removing the solution with secondary antibody and anti-actin antibody, the samples were washed by PBS for 3-5 times and DPAI solution was used to stain the nucleus for 10 minutes.

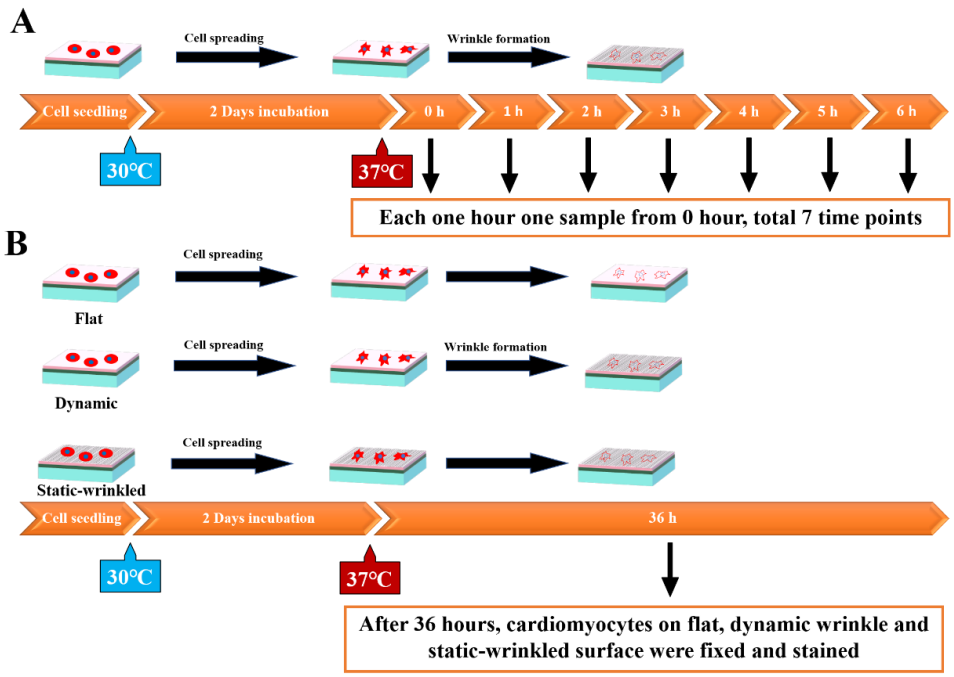


**Figure 22** Schematics showing the design of cell seeding. (A) The timeline experiments and (B) the baseline experiments.

### 2.4.3. Measurement and Analyses

Fluorescent images of cardiomyocytes were captured using a 40× oil objective on a Nikon microscope. The brightfield channel was used to determine the direction of wrinkles and the fluorescent channels were used for examining the different components of cardiomyocyte **(Figure 23 A**).

The length of focal adhesion components measurement was shown in **Figure 23 B-C**. The directions of focal adhesion components were measured via the relative angle between the stained protein and wrinkle direction **(Figure 23 B**). The relative fluorescence intensity of focal adhesion components was processed using Fiji image J (**Figure 23 C**). A square box with an area of 0.91 $\mu m^2$ (9*9, 81 pixels) was used to measure the fluorescent intensity. Then, we took the measurement value divided by the background value, and we got the relative

fluorescence intensity. The background value of each sample was defined as the measured fluorescence intensity value of the 9*9 square area which did not have cells or debris.

The costamere analyses were carried out using Fiji image J. The fluorescent images were converted to 8-bits and then binarization processing after thresholding (**Figure 23 E**). The binary images were then used to cell-adhesion counting via particle analysis. The number of costameres was counted manually based on the colocalization of binary image and actin staining (**Figure 23 F-G**).

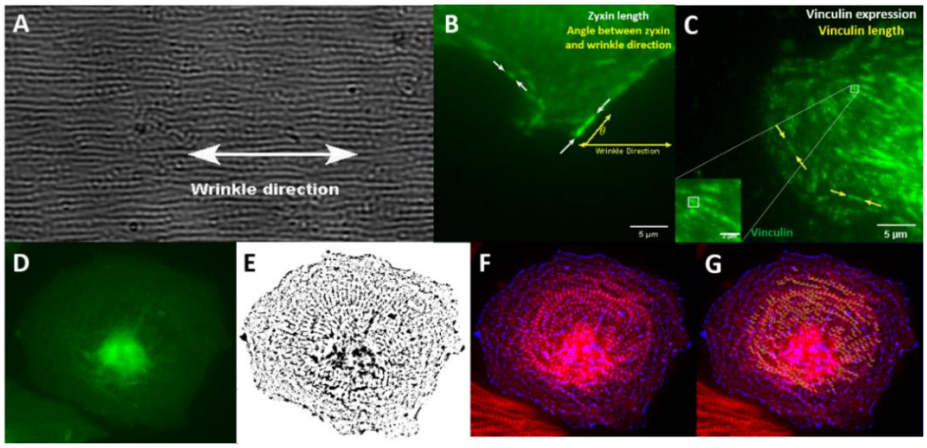


**Figure 23** Measurements of focal adhesion component. A, Bright field image, double arrow shows wrinkle direction; B, zyxin fluorescent image, θ stands for the angle between zyxin and wrinkle direction. Length between two white arrows is the length of zyxin; C, Fluorescent intensity of vinculin, insert is the amplification of measure box area. Length between two yellow arrows is the length of vinculin. D-G, flow of image processing in Fiji image J for costamere analysis**.**

### 2.4.4. Statistical Analysis

Data were analyzed using the software Prism 6 (version 6.01). One-way ANOVA with multiple comparisons was used to test the difference among groups. P-value less than 0.05 was considered a significant difference. The orientation distribution analysis using the polar graph and the violin plots were carried out by OriginPro 2020.

# 3. Results

## 3.1. Overall

To illustrate the alterations of focal adhesions and costameres in hiPSC-CMs caused by the dynamic wrinkle surface, the baseline experiments were performed first. The polymers with the static flat, static wrinkled, and dynamic wrinkle surfaces were used as substrates. hiPSC-CMs were allowed to spread for 2 days on all three groups of substrates at 30 ℃. Then all the samples were moved to 37 ℃ incubation for another 36 hours with media refreshment.

Further, to investigate the focal adhesion dynamics responding to the substrate dynamic topographical change at the initial stage temporally, we practiced the timeline experiments. The hiPSC-CMs were seeded on stretched SMPs with PEM coating and Geltrex coating for wrinkle formation and cell attachment, respectively. Similar to the baseline experiment, the hiPSC-CMs were cultured on the dynamic substrate (flat) at 30 ℃. After 2 days of spreading, the culture temperature was increased to 37 ℃ for triggering polymer recovery and wrinkle formation, which is the first timepoint (hour 0). Within the next 6 hours, samples were collected every 1 hour, which produced a total of 7 timepoints.

Samples of baseline and timeline were then fixed. Paxillin, vinculin, and zyxin were stained for tracking the changes from three layers of focal adhesion responding to substrate changes. The F-actin was co-stained with different focal adhesion components to localize the focal adhesions and costameres (**Figure 24-26**). Based on the immunostaining images, the focal adhesion dynamics were characterized by orientation distribution, length, intensity, and focal adhesion density, while costamere dynamics were characterized by costamere density and ratio of the costamere density to the total focal adhesion density.

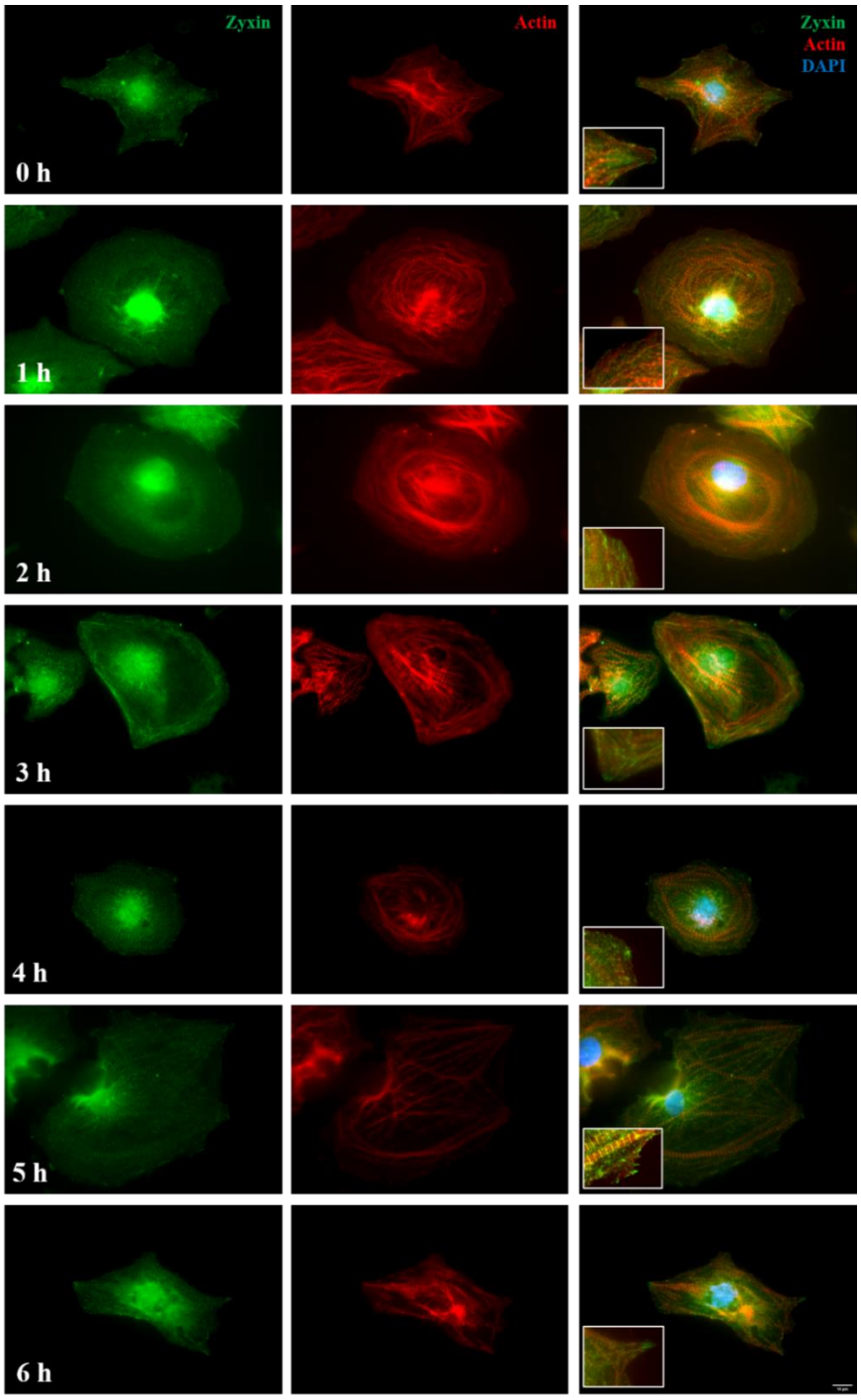


**Figure 24** Fluorescent images of zyxin. Fluorescent staining of hiPSC-CMs at different time points, including zyxin (green), F-actin (red) and DAPI (blue) from hour 0 to hour 6 after triggering wrinkle formation. The inserts show the co-localization of zyxin focal adhesions and F-actins. Scale bar, 10 μm.

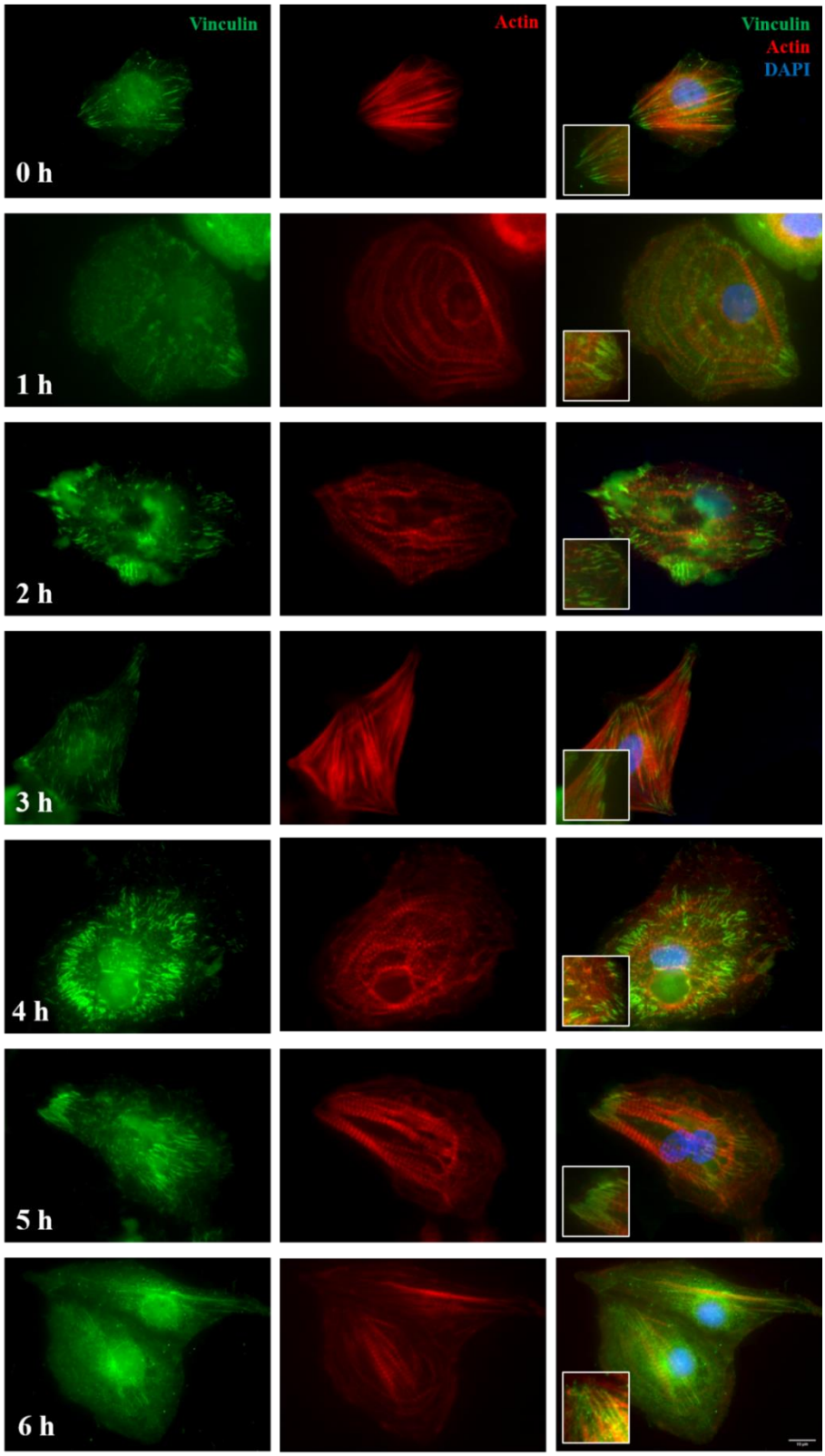


**Figure 25** Fluorescent images of vinculin. Fluorescent staining of hiPSC-CMs at different time points, including vinculin (green), F-actin (red) and DAPI (blue) from hour 0 to hour 6 after triggering wrinkle formation. The inserts show the co-localization of vinculin focal adhesions and F-actins. Scale bar, 10 μm.

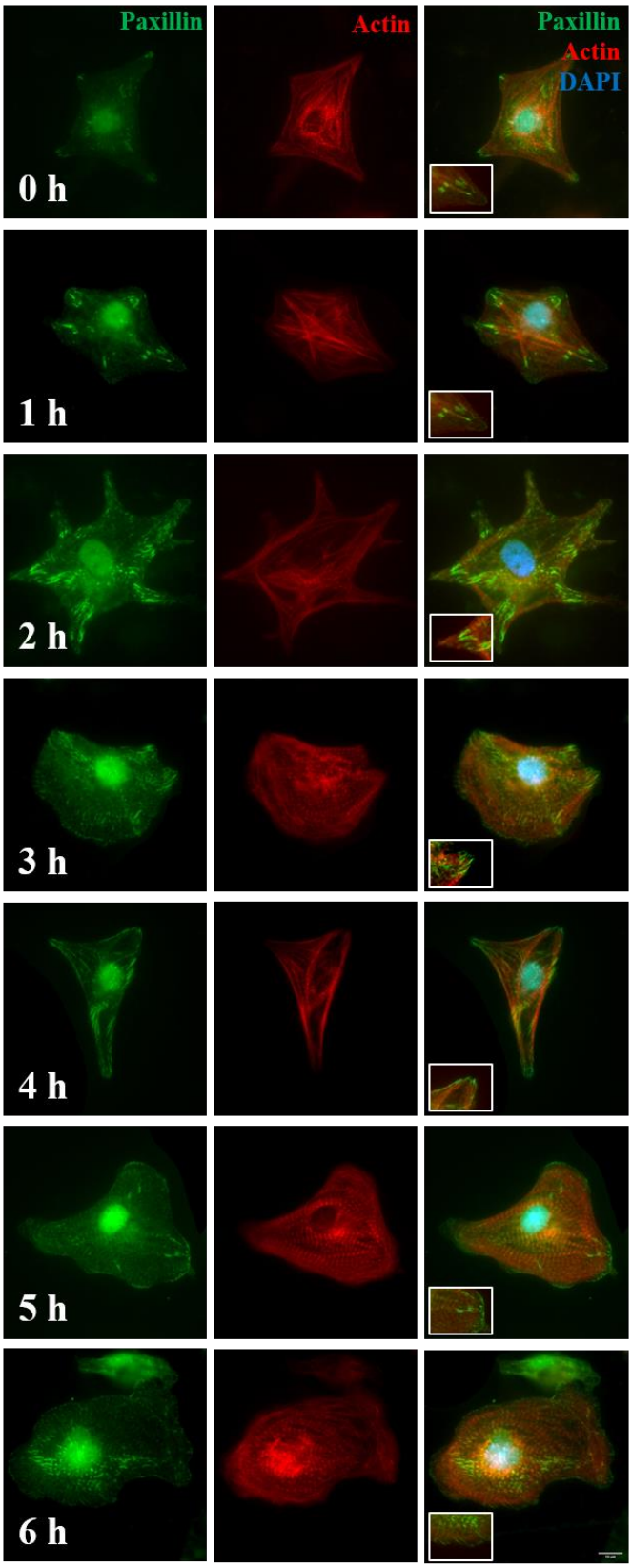


**Figure 26** Fluorescent images of paxillin. Fluorescent staining of hiPSC-CMs at different time points, including paxillin (green), F-actin (red) and DAPI (blue) from hour 0 to hour 6 after triggering wrinkle formation. The inserts show the co-localization of paxillin focal adhesions and F-actins. Scale bar, 10 μm.

### 3.2. Paxillin focal adhesions and costameres on dynamic wrinkle surface

To investigate how the dynamic wrinkle surface altered the paxillin in focal adhesions and costameres, we first tested the angle between the paxillin focal adhesions and the wrinkle direction. The result of baseline experiments showed that the paxillin orientation distribution on the static flat surface was random, and the portion of paxillin within 0°~30° was 30.8%. However, on the static wrinkled surface and dynamic wrinkle surface, the portions of paxillin within 0°~30° were 49.5% and 59.4%, respectively, which indicated that the paxillin focal adhesions were oriented to grow along the wrinkle direction after 36 hours of culturing on the dynamic wrinkle surface and static wrinkled surface (**Figure 27 A**).

Then we measured the length of paxillin in cell edge based on the immunofluorescent images. The results showed no significant difference among the three groups (**Figure 27 B**). Since there was no alteration on focal adhesion length, we further examined the fluorescence signal intensity of paxillin in focal adhesion areas to measure the *in situ* expression of paxillin in focal adhesions. To eliminate the background noise from the SMP-PEM coating and staining processes, we measured the intensity signal of the background where there existed no visible cell structure stained in every piece of the polymer as the “base line” and calculated the relative fluorescent intensity of focal adhesion sites based on the base line. The results showed that there was no significant difference between static and dynamic surfaces (**Figure 27 C**). Similarly, the total paxillin focal adhesion density, paxillin costamere density, ratio of paxillin costamere density to total paxillin focal adhesion density, and ratio of paxillin costamere to sarcomere also showed no significant difference among all three groups after 36 hours culturing (**Figure 27 D-G**).

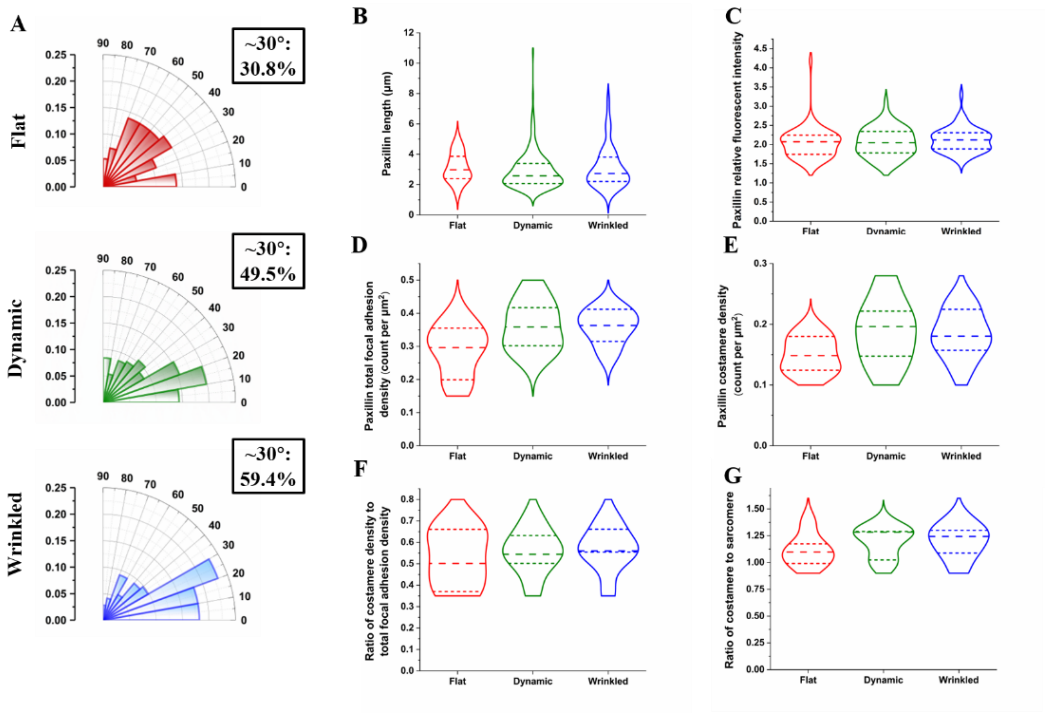


**Figure 27** Baseline results of paxillin. (A) Orientation distribution of paxillin focal adhesion on static and dynamic surfaces. (B) Length of paxillin focal adhesions. (C) Relative intensity of paxillin in focal adhesions. (D) Paxillin focal adhesion density. (E) Paxillin costamere density. (F) Ratio of paxillin costamere density to paxillin total focal adhesion density (G) Ratio of paxillin costamere number to sarcomere number.

### 3.3. Paxillin dynamics in focal adhesions and costameres

Next, with a focus on paxillin dynamics, we practiced the timeline experiments to study how paxillin responds to the dynamic wrinkle surface from hour 0 to hour 6. The orientation distribution results showed that at hour 0, when there was no wrinkle on the substrate's surface, the orientation distribution of paxillin was isotropic. After hour 3, the paxillin orientation distribution shifted from isotropic to anisotropic. The portions of paxillin within 0°~30° at hour 3 and hour 6 were 53.9% and 54.1%, which indicated the obvious reorientation of paxillin directions happened at the 3$^{rd}$ hour after triggering wrinkle formation (**Figure 28 A**).

To investigate how the dynamic wrinkle surface induced the reorientation of paxillin focal adhesions that grew along the wrinkle direction, we measured the length of paxillin in focal adhesions. We found the trend that focal adhesion length on dynamic wrinkle surface decreased first and then increased. The tremendous decrease occurred as soon as the substrate topographic change happened and kept decreasing until hour 3, while the recovery of paxillin focal adhesions to the original level occurred from hour 3 to hour 5 (**Figure 28 B**).

Given the clue presented by the above results that the reassembly of paxillin in focal adhesions started at hour 3, we then would like to examine whether the reassembly completed at hour 5 when the length recovered to the original level. The relative fluorescence intensity was quantified to illustrate the expression of paxillin in focal adhesions. We found that the paxillin intensities decreased sharply after triggering wrinkle formation ($p < 0.0001$). The lowest point was at hour 3, which was consistent with the result of the length. The relative intensity at hour 6 was still significantly lower than hour 0 (**Figure 28 C**).

The numeric change of total paxillin focal adhesion was represented by total paxillin focal adhesion density. We found that the focal adhesion density of paxillin showed no significant difference among groups (**Figure 28 D**). Costameres are the sites where Z-lines link to the cell membrane. We then examined how costameres responded to the dynamic wrinkled surface. Similarly, we examined the density of paxillin in costameres to reveal the dynamic formation of costameres from hour 0 to hour 6. The result of costamere density also showed no significant difference between groups. However, the data showed that the trend of paxillin costamere density was decreased from hour 0 to hour 3 and increased from hour 4 to hour 6 (**Figure 28 E**). To clear the relationship of costamere dynamics and total focal adhesions, we

then divided the costamere density by total focal adhesion density. The results indicated that the value at hour 3 was significantly lower than hour 0 ($p < 0.05$), which might be credit to the slight increase of total focal adhesion density and decrease of costamere density at hour 3 (**Figure 28 F**). Also, the ratio of the paxillin costamere number to the sarcomere number was tested to examine the contraction characteristics of hiPSC-CMs on the dynamic substrates. The results showed no significant difference among groups (**Figure 28 G**).

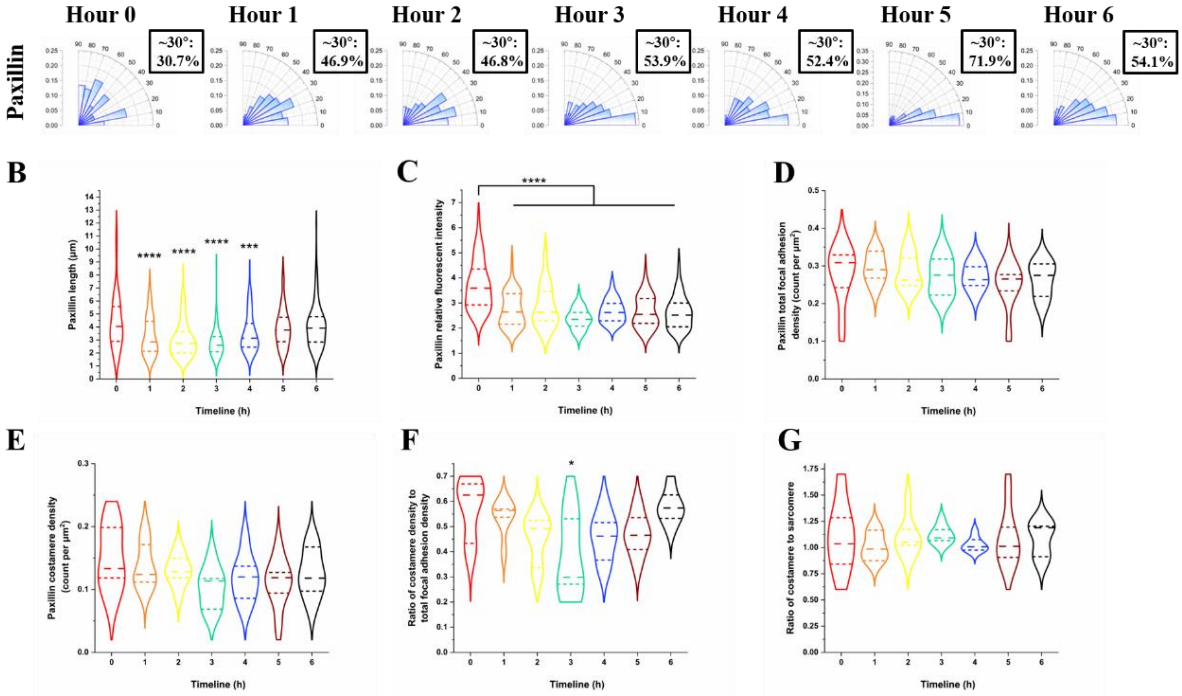


**Figure 28** Timeline results of paxillin. (A) Orientation distribution of paxillin focal adhesions on dynamic wrinkle surface after triggering wrinkle formation, the portion within 30° was labeled in each group. (B) Length of paxillin focal adhesions. (C) Relative intensity of paxillin in focal adhesions. (D) Paxillin total focal adhesion density. (E) Paxillin costamere density. (F) Ratio of paxillin costamere density to paxillin focal adhesion density. (G) Ratio of paxillin costamere number to sarcomere number *$p < 0.05$, **$p < 0.01$, ***$p < 0.001$ and ****p < 0.0001.

### 3.4. Vinculin focal adhesions and costameres on dynamic wrinkle surface

The portions of vinculin within 0°~30° on the static flat surface, dynamic wrinkle surface,

and static wrinkled surface were 33.3%, 56.1%, and 46.7%, respectively. The results indicated that vinculin proteins in focal adhesions were oriented to grow along the direction of the wrinkle after 36 hours of incubation on the dynamic wrinkle surface and static wrinkled surface (**Figure 29 A**).

The length result of vinculin focal adhesion showed no significant difference among three groups (**Figure 29 B**). In the fluorescence intensity analysis, we found that the relative intensity of vinculin focal proteins was highest on static wrinkled surface, while no significant difference was observed between the static flat surface and dynamic wrinkle surface (**Figure 29 C**). In the analyses of costameres, the total focal adhesion density, costamere density, ratio of costamere number to sarcomere number, and ratio of costamere density to total focal adhesion density of vinculin all showed no significant difference among groups after 36 hours of culturing (**Figure 29 D-G**).

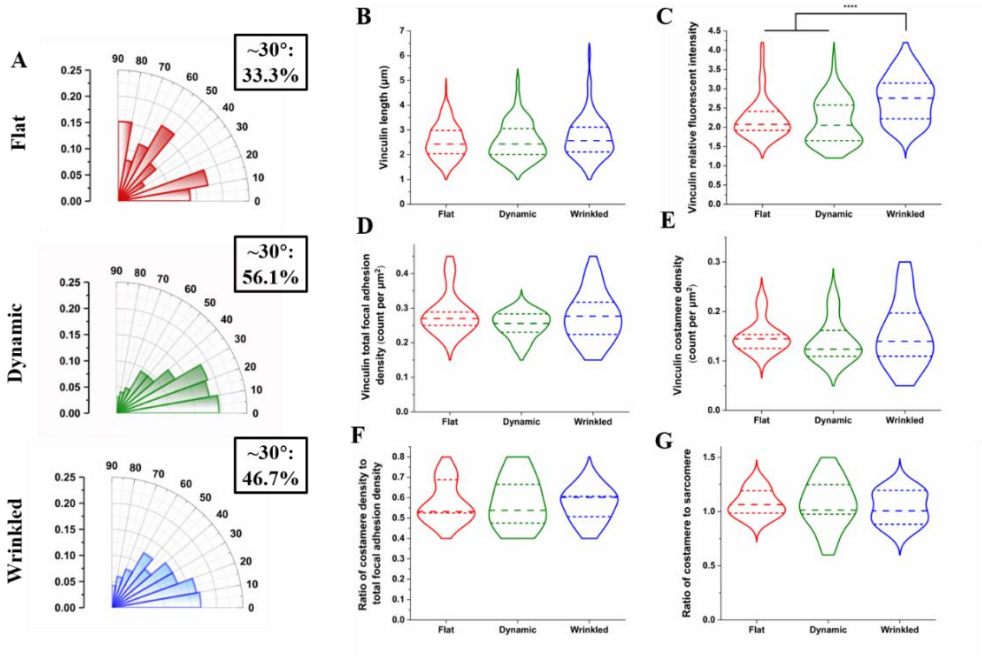


**Figure 29** Baseline results of vinculin. (A) Orientation distribution of vinculin focal adhesion on static and dynamic surfaces. (B) Length of vinculin focal adhesions. (C) Relative intensity of vinculin in focal adhesions. (D) Vinculin focal adhesion density. (E) Vinculin costamere

density. (F) Ratio of vinculin costamere density to vinculin total focal adhesion density (G) Ratio of vinculin costamere number to sarcomere number. ****$p < 0.0001$.

### 3.5. Vinculin dynamics in focal adhesions and costameres

Next, we focused on the vinculin dynamics in focal adhesions and costameres responding to the dynamic wrinkle surface within the first 6 hours after triggering wrinkle formation. We first measured the orientation distributions of vinculin from hour 0 to hour 6. The results indicated that the vinculin focal adhesion distribution was isotropic at hour 0. The portions of vinculin within 0°~30° from hour 4 to hour 6 were 45.9%, 52.0% and 38.5%, respectively. The results indicated that the vinculin focal adhesions were also reoriented, but the reorientation was not as obvious as paxillin in the first 6 hours (**Figure 30 A**).

The length results of vinculin showed a similar pattern as the paxillin did. The trend of vinculin focal adhesion length was decreased first and then increased. While the length at hour 1 was significantly shorter than hour 0 ($p = 0.025$), the tremendous decrease of focal adhesion length started from hour 2 ($p < 0.0001$). At hour 3, it reached the lowest point, then started to recover. At hour 6, the vinculin focal adhesions were still extremely shorter than hour 0 (**Figure 30 B**). The relative intensity of vinculin focal adhesions from hour 0 to hour 6 on the dynamic wrinkle surface were analyzed as well. Interestingly, the pattern of vinculin focal adhesion was unlike the paxillin, and the intensity of vinculin at hour 2 was significantly higher than hour 0 ($p = 0.0034$). The highest point was at hour 4 ($p < 0.0001$), then the relative intensity of vinculin was decreased and came back to its original level at hour 6 (**Figure 30 C**).

The numeric measurement of total focal adhesions containing vinculin protein was performed

as well based on the vinculin staining images. The results indicated that at hour 4~6, the vinculin total focal adhesion densities were significantly larger than hour 0 (**Figure 30 D**). To find out how the increase happened, we then quantified the costamere density by colocalizing with sarcomeric actin staining. Though the results showed no significant difference among groups, it had the trend of decreasing at hour 0~3, then increasing at hour 4~6 (**Figure 30 E**). The pattern of ratio of costamere density to total focal adhesion density decreased from hour 0~3 and then increased from hour 4~6. From hour 1 to hour 6, the values were significantly smaller than hour 0, which was contributed by the increase of total focal adhesion density and the trend of costamere densities (**Figure 30 F**). Also, the ratio of vinculin costamere number to sarcomere number was examined and the results showed no significant difference among groups (**Figure 30 G**).

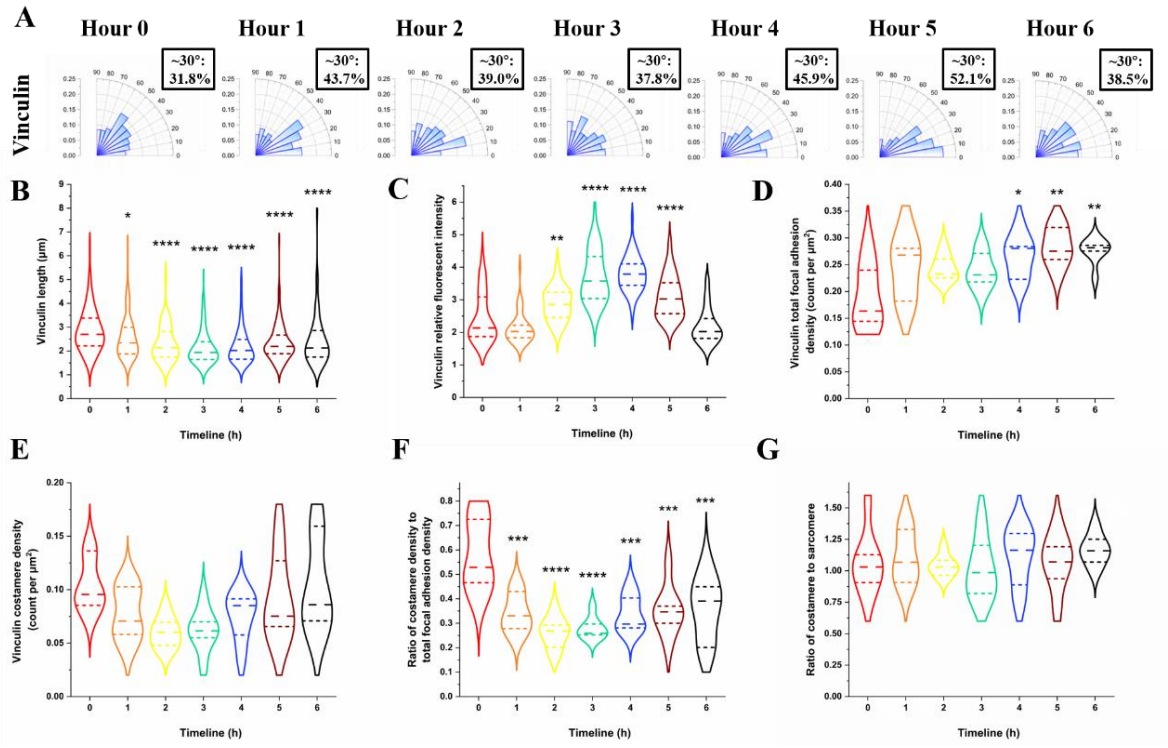


**Figure 30** Timeline results of vinculin. (A) Orientation distribution of vinculin focal adhesions on dynamic wrinkle surface after triggering wrinkle formation, the portion within 30° was labeled in each group. (B) Length of vinculin focal adhesions. (C) Relative intensity of vinculin in focal adhesions. (D) Vinculin total focal adhesion density. (E) Vinculin costamere density. (F) Ratio of vinculin costamere density to vinculin total focal adhesion

density. (G) Ratio of vinculin costamere number to sarcomere number *$p < 0.05$, **$p < 0.01$, ***$p < 0.001$ and ****$p < 0.0001$.

### 3.6. Zyxin focal adhesions and costameres on dynamic wrinkle surface

Finally, we tested the behavior of zyxin protein (from the actin regulatory layer) in focal adhesions and costameres on dynamic wrinkle surface. The orientation distributions of zyxin focal adhesions on static and dynamic surfaces were tested firstly. The results showed that the portions of zyxin focal adhesions within 0°~30° were 42.5%, 52.8%, and 52.6% on the static flat surface, dynamic wrinkle surface, and static wrinkled surface after 36 hours culturing, respectively (**Figure 31 A**). The results of orientation distribution suggested that the zyxin focal adhesion also shows the preference of growing along with the wrinkle directions on dynamic wrinkle surface and static wrinkled surface after 36 hours of culturing.

The length measurement showed that the zyxin focal adhesions on static wrinkled surfaces were longer than the dynamic wrinkle surface, while no significant difference was observed between the static flat surface and dynamic wrinkle surface (**Figure 31 B**). The relative fluorescence intensities of zyxin focal adhesions on dynamic wrinkle surface and static wrinkled surface were significantly higher than the static flat surface ($p < 0.0001$) (**Figure 31 C**). The total focal adhesion density of zyxin proteins showed that the zyxin total focal adhesion density on the static wrinkled surface was significantly lower than it on the static flat surface, while there was no significant difference between dynamic and static surfaces (**Figure 31 D**). For the analyses of zyxin costamere density, the ratio of costamere density to total focal adhesion density, and ratio of costamere number to sarcomere number were examined, the results showed no significant difference among three groups (**Figure 31 E~G**).

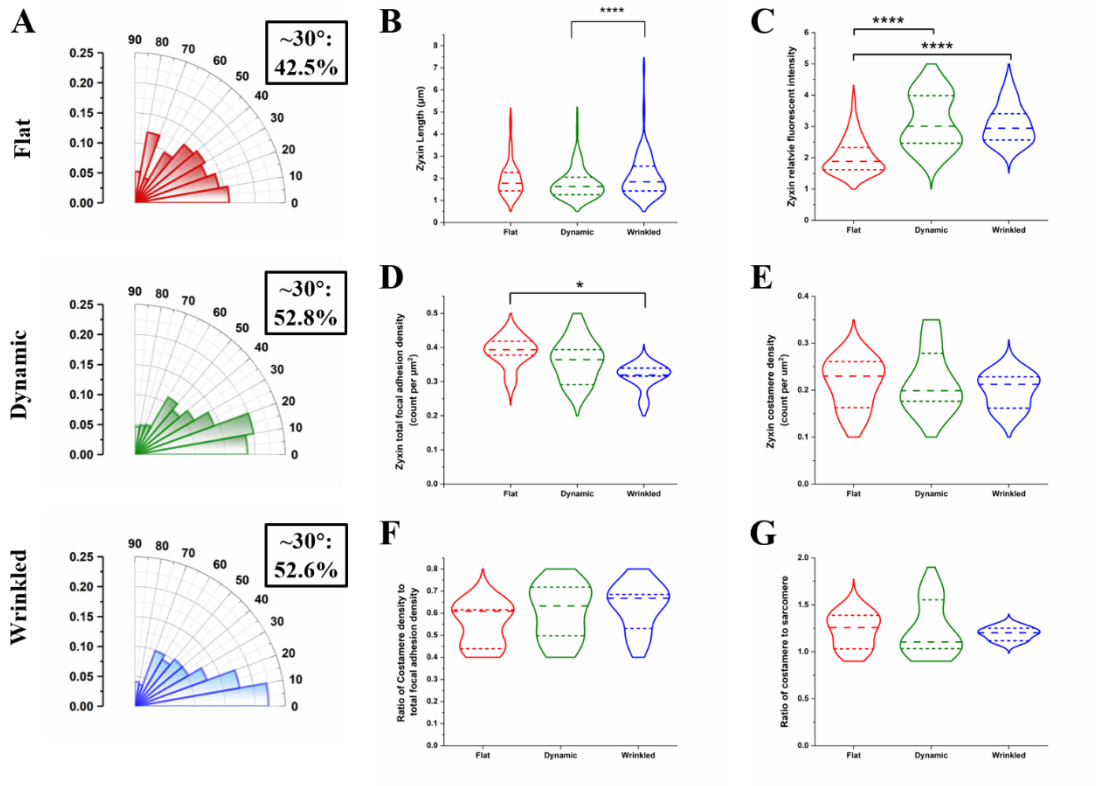


**Figure 31** Baseline results of zyxin. (A) Orientation distribution of zyxin focal adhesion on static and dynamic surfaces. (B) Length of zyxin focal adhesions. (C) Relative intensity of zyxin in focal adhesions. (D) Zyxin focal adhesion density. (E) Zyxin costamere density. (F) Ratio of zyxin costamere density to zyxin total focal adhesion density (G) Ratio of zyxin costamere number to sarcomere number. *$p < 0.05$, ****$p < 0.0001$.

### 3.7. Zyxin dynamics in focal adhesions and costameres

Similarly, we performed timeline experiments to examine the dynamics of focal adhesion actin regulatory layer responding to the dynamic change of the substrate. The results of the orientation distribution showed that the portion of zyxin within 0°~30° was 25.2% at hour 0. From hour 0 to hour 6, the portion of 0°~30° were all below to 40%, which indicated that the zyxin did not reorient along the wrinkle direction in the first 6 hours responding to the dynamic change of the substrate (**Figure 32 A**).

No significant length change was found on zyxin proteins comparing hour 1~6 to hour 0;

however, the length results showed the trend that it decreased from hour 0 to hour 3, and then it increased. At hour 3, the length of zyxin protein was shortest, which was significantly shorter than hour 5 and hour 6 ($p = 0.0022$, $p = 0.0023$, respectively). While the length at hour 4 was slightly longer than it was at hour 3, it was still significantly shorter than it was at hour 5 and hour 6 ($p = 0.043$, $p = 0.038$, respectively) (**Figure 32 B**). The results of zyxin focal adhesion relative fluorescent intensity were similar to the length results. Though the values were fluctuant, we can still observe the slight trend that it decreased first and then increased. The relative intensity at hour 2 was significantly lower than it was at hour 0, while at hour 6 the relative intensity was significantly higher than hour 0 (**Figure 32 C**).

The total focal adhesion density of zyxin showed that the hiPSC-CMs did not initiate more zyxin focal adhesions comparing hour 1~6 to hour 0. However, the densities at hour 4~6 were significantly lower than hour 1 and the hour 3~6 were significantly higher than hour 2 (**Figure 32 D**). To detail the pattern found in total focal adhesion density, the costamere densities of zyxin within the first 6 hours after triggering wrinkle formation were also measured. No significant difference was observed between different groups (**Figure 32 E**). The ratio of costamere density to total focal adhesion density of zyxin results showed no significant difference comparing hour 1~6 to hour 0. However, we found the trend that it decreased firstly and then increased. The values at hour 1 and hour 2 were significantly smaller than hour 5 and hour 6, respectively (**Figure 32 F**). The costamere number and sarcomere number were also examined and the ratio of the costamere number to the sarcomere number was calculated to analyze the interaction between contraction units and zyxin costameres. The results showed that the values from hour 0 to hour 6 were fluctuant, but no significant difference was observed between groups (**Figure 32 G**).

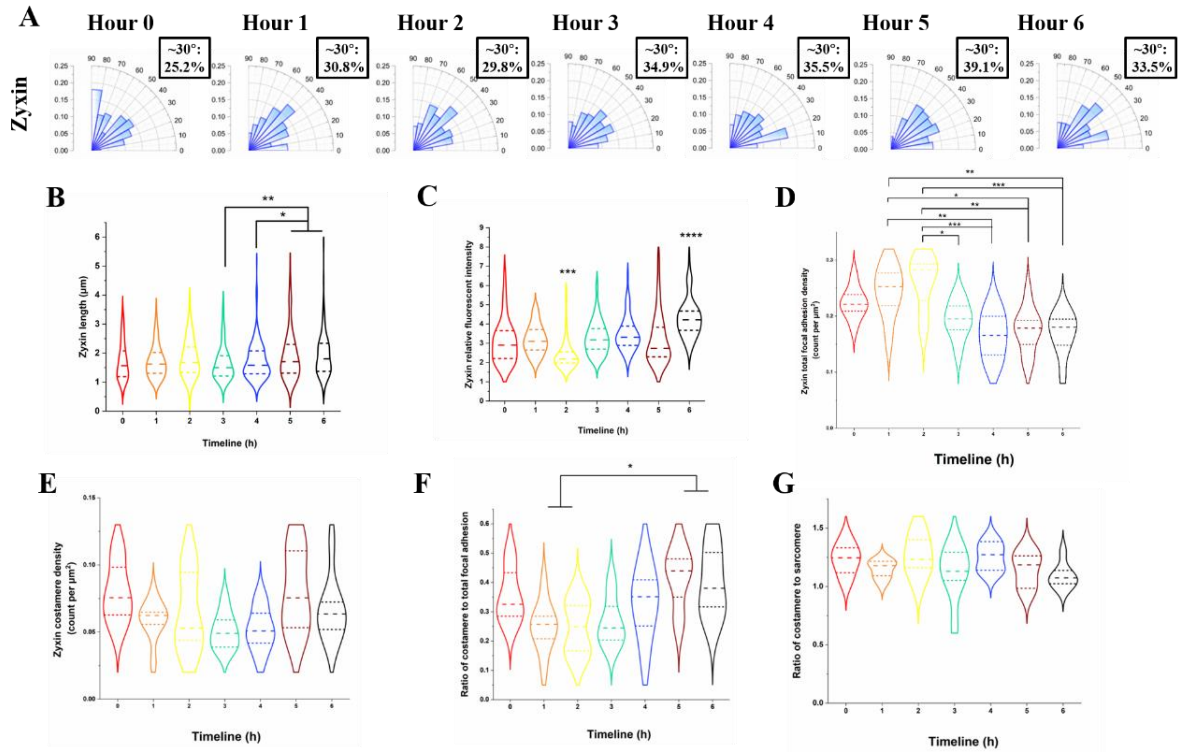


**Figure 32** Timeline results of zyxin. (A) Orientation distribution of zyxin focal adhesions on dynamic wrinkle surface after triggering wrinkle formation, the portion within 30° was labeled in each group. (B) Length of zyxin focal adhesions. (C) Relative intensity of zyxin in focal adhesions. (D) Zyxin total focal adhesion density. (E) Zyxin costamere density. (F) Ratio of zyxin costamere density to zyxin total focal adhesion density. (G) Ratio of zyxin costamere number to sarcomere number *$p < 0.05$, **$p < 0.01$, ***$p < 0.001$ and ****$p < 0.0001$.

# 4. Discussion

In this study, the length results of paxillin, vinculin, and zyxin all showed the trend of decreasing first and then increasing, which suggested that the disassembly and reassembly of focal adhesions occurred responding to the dynamic substrates during the first 6 hours. The paxillin existing in the integrin signaling layer responded to the change of substrate first, followed by the vinculin. The alteration of zyxin was not as obvious as paxillin and vinculin. The result of paxillin's relative intensity showed that the reassembly of paxillin was not incomplete at hour 6. It has been reported that the spatial distribution of vinculin could be

effectively altered by the absence of paxillin[63]. In this study, we found the vinculin involved in focal adhesions showed higher intensity from hour 2 to hour 5 compared to hour 0, which may lead by the decrease of paxillin length. When the paxillin binding sites were insufficient, the vinculin aggregated more in the force transition layer and actin regulatory layer than the ones under normal conditions. The insufficient paxillin binding sites contributed to the decrease in vinculin length as well as the increase in intensity. According to a previous report, the zyxin accumulation in focal adhesions is related to the mechanical load on focal adhesions[64]. In this study, we also observed that the intensity of zyxin decreased from hour 0~3, which may account for the deduction of mechanical load caused by the instability of focal adhesion structures.

The total focal adhesion densities of paxillin were not altered significantly, which suggested the paxillin did not passively initiate more sites for paxillin focal adhesions and costameres growing responding to wrinkle formation of substrates. The total focal adhesion densities of vinculin at hour 4~6 were significantly higher than hour 0, but according to the baseline results, there was no significant difference among three groups after 36 hours. The results of total focal adhesion density in timeline and baseline suggested that the vinculin focal adhesion dynamics were still ongoing at hour 6; the hiPSC-CMs might experience the process that reduces the focal adhesion sites or extend the cell spreading for vinculin total focal adhesion density decreasing back to the original level after hour 6, which was also consistent with the result of vinculin length that reorganization of vinculin focal adhesion was not finished at hour 6. The costamere density of zyxin, vinculin, and paxillin all showed the slight trend that decreases from hour 0 to hour 3 and increases from hour 4 to hour 6, which suggested the costamere formations were affected by the dynamic substrate as well. It has been reported that the FAK is essential for cell responses toward substrate topography[65].

Moreover, the activities of FAK are closely relative to the turnover of focal adhesion complexes[66,67]. The observations of focal adhesion disassembly and reassembly induced by dynamic substrates in our studies may also relate to the activities of FAK.

We also measured the ratio of the costamere number to the sarcomere number to find out the relationship between the cell contraction units and the protein complexes mediating the force conduction. No significant difference was observed during the first 6 hours after triggering wrinkle formation in all three groups, which might suggest that, during this process, the effects of substrate change had not been translated into the change of cell beating. Interestingly, we found that there were more costameres than sarcomeres in the cells. This phenomenon was ubiquitous at different time points, which may account for the existence of M-line costameres. The M-line costameres are first reported in 1992[68], but the research on M-line costameres is limited. In this study, we found that the M-line costameres existed in all three proteins and the M-line costameres were dimmer than Z-line costameres (**Figure 33**). This finding may guide the direction of future research about the differences and relationships between Z-line costameres and M-line costameres.

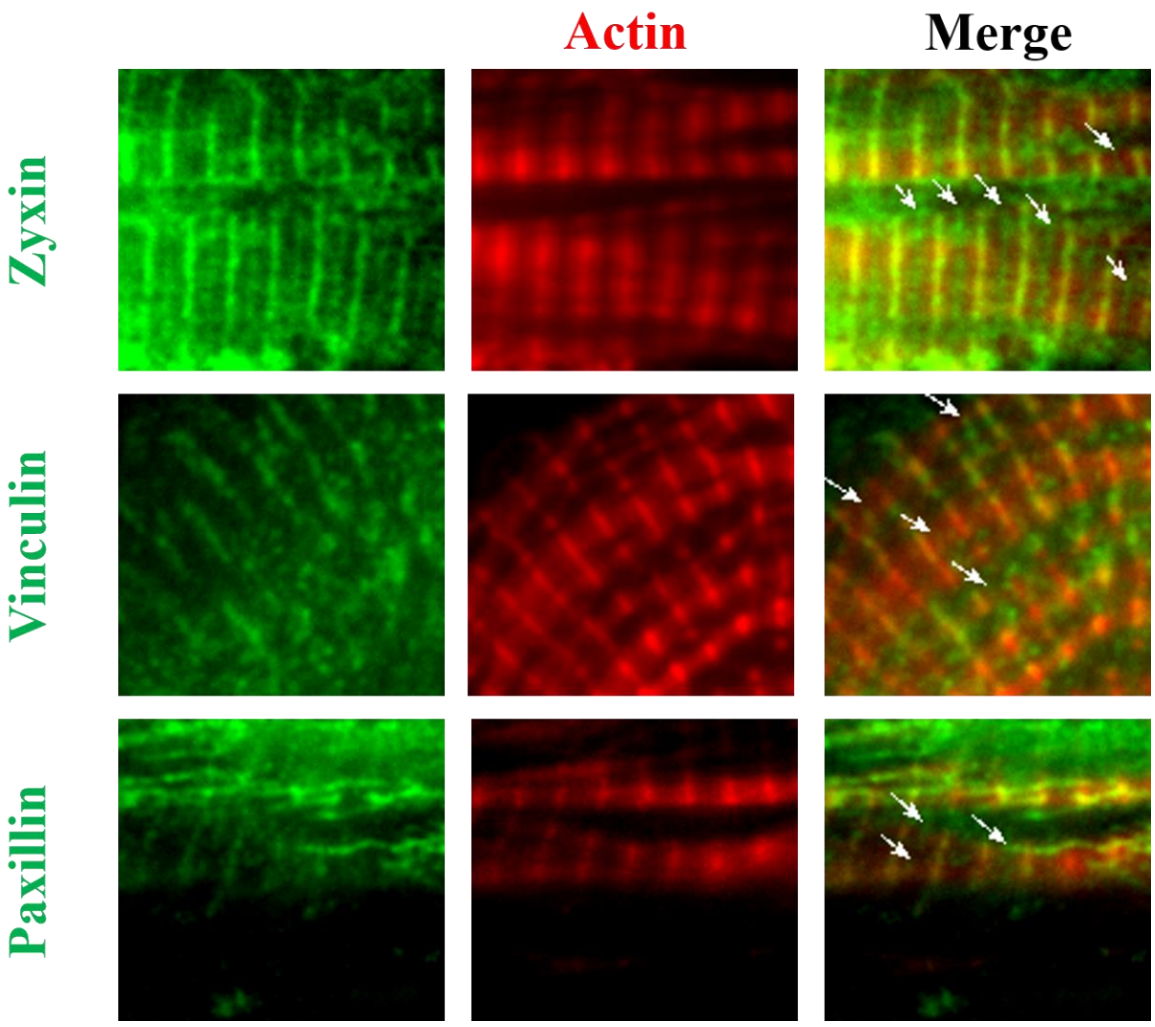


**Figure 33** M-line costameres. Fluorescent images showing the co-staining of costamere components (zyxin, vinculin and paxillin) and F-actin. The white arrows in merged images show the M-line costamere.

# 5. Future Work

To understand how focal adhesion architectures are assembled in response to the dynamic wrinkle surface, in future studies, the gene expression of focal adhesion proteins should be examined temporally. In this study, we found that the focal adhesion experienced disassembly in the first 6 hours. It has been reported that the phosphorylation of FAK on Tyr 397 will accelerate the disassembly of FA complex[69]. Also, it has been observed that the

inhibition of FAK can prevent the activation of YAP[70]; on the other hand, the YAP mutant cell line showed a marked reduction in FAK autophosphorylation on Tyr 397[14]. Thus, it is rational to make the hypothesis that the focal adhesion disassembly in the first 6 hours on dynamic wrinkle surface was mediated by the activation of Try 397 FAK, and the p-FAK (397) was prompted by the activation of YAP that was triggered by the ECM mechanical cues. In future research, we can stain the YAP and p-FAK (397) to examine the *in situ* deposition of YAP and p-FAK. Also, the western blot could be performed to quantify the amount of p-FAK (397) and YAP of CMs at each timepoint.

The focal adhesions are associated with the functionalization of CMs, so the functional tests of CMs responding to dynamic wrinkle surfaces should be practiced as well. The indexes related to costameres should be detailed to examine the costamere dynamics and the relationship between costamere dynamics and CM contractions. Drug treatment using an FAK inhibitor should be performed. The FAK inhibitor 14 (Y15) can inhibit the autophosphorylation of FAK at Try 397. The experiment may start with tracking how proteins in focal adhesion architecture respond to the Y15 treatment on a flat surface. To perform timeline experiments on dynamic wrinkle surfaces, we would seed the CMs on strained SMP-PEM substrates and allow CMs to spread for 2 days at 30 ℃. At this point, upon triggering wrinkle formation, the Y15 should be added into the medium simultaneously, which is the first time point (hour 0). In the subsequent 6 hours, samples were collected every hour to analyze how focal adhesions behave in response to the chemical inhibitor and dynamic substrate. Besides the behavior of focal adhesions, we may also examine the YAP expression under the treatment of Y15 to investigate how the YAP pathway reacts to the joint efforts of substrate topographic change and chemical inhibition.

In this study, the intensity of vinculin has been recorded to be unidentical to the pattern of paxillin proteins responding to dynamic wrinkle surface; in future research, how the accumulations of proteins from the force transduction layer and actin regulatory layers change along the Z-axis should be studied. To be specific, the paxillin and vinculin will be co-stained, and 3D confocal images of CMs will be performed. The fluorescence signal intensity of paxillin in the Z-axis should be examined first. We may need to dye the substrate surface so that we can measure the relative distance between the paxillin and ECM, and the distance between vinculin and ECM. We found that the focal adhesions disassembly and reassembly were in the first 6 hours responding to the dynamic wrinkle surface in this study. Therefore, we will do the Z scanning to the samples at each hour within these first 6 hours to test the accumulation distributions and distance of paxillin and vinculin in focal adhesions along the Z-axis relative to the ECM. We may need to knockout paxillin to investigate how the deficiency of paxillin changes the behavior of vinculin on both flat and dynamic wrinkle surfaces.

We found the M-line costameres in vinculin, paxillin, and zyxin staining in CMs. The M-line costamere is dimmer than Z-line costameres, and the total number of M-line costamere is less than the Z-line costameres based on the immunofluorescent images. The studies on the difference between Z-line and M-line costameres are still poorly understood. Also, the specific functions of Z-line and M-line costameres are unknown. One study on costamere structure with integrin β1D staining[71] enlightens us that there might be some difference in integrins between Z-line costameres and M-line costameres. In the future study, we may need to do more staining about integrins and ECM.

The actin or α-actinin could be stained to localize the position of Z-lines, while the myomesin

could be stained for localizing the position of M-lines. The images could be analyzed using the 'intensity profile' function in ImageJ. By using the intensity profile, we can get the data about the average distance between costameres, sarcomere length, fluorescent intensity of M-line costameres and Z-line costameres. We found that the M-line costameres are dimmer than the Z-line costameres. Moreover, the M-line costameres are more obvious in zyxin staining than in vinculin and paxillin staining (**Figure 33**). This phenomenon brings up the questions whether a protein (i.e. vinculin, paxillin) in the M-line costameres and the same protein in the Z-line costameres have the same relative distance between ECM. On the other hand, do the M-line costameres, like focal adhesions and Z-line costameres, directly link with the ECM?

We may address these questions by using the Z-direction scanning of the costameres. The protein existing in both M-line costameres and Z-line costameres (i.e. paxillin, vinculin, zyxin, talin) can be co-stained with actin/α-actinin or myomesin. 3D confocal images of CMs with fluorescent ECM should be collected to examine the relative distance between ECM and different components in the M-line and the Z-line costameres. It has been reported that during the maturation of cardiomyocytes, the α5 integrins would be replaced by α7 integrins[72], since the α7 integrins are laminin receptors while α5 integrins are fibronectin receptors. We can coat the substrate with different fluorescent-probe-labeled ECM proteins, either laminin or fibronectin, together with the staining of integrin α5 or integrin α7, a super resolution microscope can be used to determine whether the integrins directly connect with ECM.

# 6. Reference


1. Lee, I. Mid-term: Study. **965**, 949–965 (1992).
2. Li, F., Wang, X., Capasso, J. M. & Gerdes, A. M. Rapid Transition of Cardiac Myocytes from Hyperplasia to Hypertrophy During Postnatal Development. **1746**, 1737–1746 (1996).
3. Ribeiro, M. C. *et al.* Biomaterials Functional maturation of human pluripotent stem cell derived cardiomyocytes in vitro e Correlation between contraction force and electrophysiology. *Biomaterials* **51**, 138–150 (2015).
4. Gerdes, A. M. *et al.* Structural Remodeling of Cardiac Myocytes in Patients With Ischemic Cardiomyopathy. 426–430
5. Composition, I. I. T. & Growth, C. Morphometric Study of Early Postnatal Development in the Left and Right Ventricular Myocardium of the Rat. (1980).
6. Dunn, K. K. & Palecek, S. P. Engineering scalable manufacturing of high-quality stem cell-derived cardiomyocytes for cardiac tissue repair. *Front. Med.* **5**, (2018).
7. Geiger, B. & Bershadsky, A. Assembly and mechanosensory function of focal contacts. 584–592 (2001).
8. Kanchanawong, P. *et al.* NIH Public Access. **468**, 580–584 (2011).
9. Kanchanawong, P. *et al.* Nanoscale architecture of integrin-based cell adhesions. *Nature* **468**, 580–584 (2010).
10. Paluch, E. K., Aspalter, I. M. & Sixt, M. Focal Adhesion – Independent Cell Migration. (2016). doi:10.1146/annurev-cellbio-111315-125341
11. Senetar, M. A., Moncman, C. L. & Mccann, R. O. Talin2 is Induced During Striated Muscle Differentiation and Is Targeted to Stable Adhesion Complexes in Mature Muscle. **173**, 157–173 (2007).

12. Fässler, R. *et al.* Differentiation and integrity of cardiac muscle cells are impaired in the absence of β 1 integrin. **2999**, 2989–2999 (1996).

13. Sathe, A. R., Shivashankar, G. V & Sheetz, M. P. Nuclear transport of paxillin depends on focal adhesion dynamics and FAT domains. 1981–1988 (2016). doi:10.1242/jcs.172643

14. Nardone, G. *et al.* YAP regulates cell mechanics by controlling focal adhesion assembly. (2017). doi:10.1038/ncomms15321

15. Taneja, N., Neininger, A. C., Bersi, M. R., Merryman, W. D. & Burnette, D. T. Focal adhesion kinase regulates early steps of myofibrillogenesis in cardiomyocytes. *bioRxiv* 261248 (2018). doi:10.1101/261248

16. Adhesions, C. *et al.* a -Actinin Drives Cardiac Sarcomere Assembly from Short Article Force Generation via b -Cardiac Myosin , Titin , and a -Actinin Drives Cardiac Sarcomere Assembly from Cell-Matrix Adhesions. *Dev. Cell* **44**, 87-96.e5 (2018).

17. Chu, M. *et al.* Serine-910 phosphorylation of focal adhesion kinase is critical for sarcomere reorganization in cardiomyocyte hypertrophy. *Cardiovasc. Res.* **92**, 409–419 (2011).

18. Domingos, P. P., Fonseca, P. M., Nadruz, W. & Franchini, K. G. Load-induced focal adhesion kinase activation in the myocardium: Role of stretch and contractile activity. *Am. J. Physiol. - Hear. Circ. Physiol.* **282**, 556–564 (2002).

19. Pardo, J. V, Siliciano, J. D. A. & Craig, S. W. A Vinculin-Containing Cortical Lattice in Skeletal Muscle : Transverse Lattice Elements ( `` Costameres ' ') Mark Sites of Attachment between Myofibrils and Sarcolemma Author ( s ): José V . Pardo , Janet D ' Angelo Siliciano and Susan W . Craig Source : P. **80**, 1008–1012 (2020).

20. Review, I. & Hoshijima, M. Mechanical stress-strain sensors embedded in cardiac cytoskeleton : Z disk , titin , and associated structures. (2020).

doi:10.1152/ajpheart.00816.2005.

21. Danowski, B. A. *et al.* Costameres Are Sites of Force Transmission to the Substratum in Adult Rat Cardiomyocytes Stable URL : https://www.jstor.org/stable/1615309 REFERENCES Linked references are available on JSTOR for this article : Costameres Are Sites of Force Transmission to. **118**, 1411–1420 (2020).

22. Mansour, H., Tombe, P. P. De, Samarel, A. M. & Russell, B. Restoration of Resting Sarcomere Length After Uniaxial Static Strain Is Regulated by Protein Kinase C ♫ and Focal Adhesion Kinase. 642–649 (2004). doi:10.1161/01.RES.0000121101.32286.C8

23. Ervasti, J. M. Costameres: The Achilles' heel of Herculean muscle. *J. Biol. Chem.* **278**, 13591–13594 (2003).

24. Peter, A. K., Cheng, H., Ross, R. S., Knowlton, K. U. & Chen, J. Progress in Pediatric Cardiology The costamere bridges sarcomeres to the sarcolemma in striated muscle. *Prog. Pediatr. Cardiol.* **31**, 83–88 (2011).

25. Fujita, H., Nedachi, T. & Kanzaki, M. Accelerated de novo sarcomere assembly by electric pulse stimulation in C2C12 myotubes. **3**, (2007).

26. Sparrow, J. C. & Schöck, F. The initial steps of myofibril assembly: Integrins pave the way. *Nature Reviews Molecular Cell Biology* **10**, 293–298 (2009).

27. Mummery, C. L. *et al.* Differentiation of human embryonic stem cells and induced pluripotent stem cells to cardiomyocytes: A methods overview. *Circulation Research* **111**, 344–358 (2012).

28. Burridge, P. W. *et al.* Chemically defned generation of human cardiomyocytes. *Nat. Methods* **11**, 855–860 (2014).

29. Batalov, I. & Feinberg, A. W. Differentiation of cardiomyocytes from human pluripotent stem cells using monolayer culture. *Biomark. Insights* **10**, 71–76 (2015).

30. Xi, J. *et al.* Comparison of contractile behavior of native murine ventricular tissue and

cardiomyocytes derived from embryonic or induced pluripotent stem cells. *FASEB J.* **24**, 2739–2751 (2010).

31. Khan, M. *et al.* Evaluation of Changes in Morphology and Function of Human Induced Pluripotent Stem Cell Derived Cardiomyocytes (HiPSC-CMs) Cultured on an Aligned-Nanofiber Cardiac Patch. *PLoS One* **10**, e0126338 (2015).
32. Sartiani, L. *et al.* Developmental Changes in Cardiomyocytes Differentiated from Human Embryonic Stem Cells: A Molecular and Electrophysiological Approach. *Stem Cells* **25**, 1136–1144 (2007).
33. Schaefer, L. & Schaefer, R. M. Proteoglycans_from_structural.PDF. *Cell and Tissue Research* **339**, 237–246 (2010).
34. Sainio, A. & Järveläinen, H. Extracellular matrix macromolecules: potential tools and targets in cancer gene therapy. *Mol. Cell. Ther.* **2**, 14 (2014).
35. Jourdan-LeSaux, C., Zhang, J. & Lindsey, M. L. Extracellular matrix roles during cardiac repair. *Life Sci.* **87**, 391–400 (2010).
36. Higuchi, S. *et al.* Heart extracellular matrix supports cardiomyocyte differentiation of mouse embryonic stem cells. *J. Biosci. Bioeng.* **115**, 320–325 (2013).
37. Weber, K. T. Cardiac interstitium in health and disease: The fibrillar collagen network. *J. Am. Coll. Cardiol.* **13**, 1637–1652 (1989).
38. Jacot, J. G., McCulloch, A. D. & Omens, J. H. Substrate stiffness affects the functional maturation of neonatal rat ventricular myocytes. *Biophys. J.* **95**, 3479–3487 (2008).
39. Xue, M. & Jackson, C. J. Extracellular Matrix Reorganization During Wound Healing and Its Impact on Abnormal Scarring. *Adv. Wound Care* **4**, 119–136 (2015).
40. Rao, C. *et al.* The effect of microgrooved culture substrates on calcium cycling of cardiac myocytes derived from human induced pluripotent stem cells. *Biomaterials* **34**, 2399–2411 (2013).

41. Sia, J., Yu, P., Srivastava, D. & Li, S. Effect of biophysical cues on reprogramming to cardiomyocytes. *Biomaterials* **103**, 1–11 (2016).

42. Wang, P. Y., Yu, J., Lin, J. H. & Tsai, W. B. Modulation of alignment, elongation and contraction of cardiomyocytes through a combination of nanotopography and rigidity of substrates. *Acta Biomater.* **7**, 3285–3293 (2011).

43. Kim, P. *et al.* Fabrication of nanostructures of polyethylene glycol for applications to protein adsorption and cell adhesion. *Nanotechnology* **16**, 2420–2426 (2005).

44. Chien, F. C., Dai, Y. H., Kuo, C. W. & Chen, P. Flexible nanopillars to regulate cell adhesion and movement. *Nanotechnology* **27**, (2016).

45. Oyunbaatar, N. E., Lee, D. H., Patil, S. J., Kim, E. S. & Lee, D. W. Biomechanical characterization of cardiomyocyte using PDMS pillar with microgrooves. *Sensors (Switzerland)* **16**, 1–13 (2016).

46. Kai, D., Prabhakaran, M. P., Jin, G. & Ramakrishna, S. Guided orientation of cardiomyocytes on electrospun aligned nanofibers for cardiac tissue engineering. *J. Biomed. Mater. Res. - Part B Appl. Biomater.* **98 B**, 379–386 (2011).

47. Prabhakaran, M. P. *et al.* Differentiation of embryonic stem cells to cardiomyocytes on electrospun nanofibrous substrates. *J. Biomed. Mater. Res. - Part B Appl. Biomater.* **102**, 447–454 (2014).

48. Fu, C. C. *et al.* Tunable nanowrinkles on shape memory polymer sheets. *Adv. Mater.* **21**, 4472–4476 (2009).

49. Luna, J. I. *et al.* Multiscale biomimetic topography for the alignment of neonatal and embryonic stem cell-derived heart cells. *Tissue Eng. - Part C Methods* **17**, 579–588 (2011).

50. Greco, F. *et al.* Microwrinkled conducting polymer interface for anisotropic multicellular alignment. *ACS Appl. Mater. Interfaces* **5**, 573–584 (2013).

51. Abadi, P. P. S. S. *et al.* Engineering of Mature Human Induced Pluripotent Stem Cell-Derived Cardiomyocytes Using Substrates with Multiscale Topography. *Adv. Funct. Mater.* **28**, 1–11 (2018).

52. Zhang, L. *et al.* Potential-Responsive Surfaces for Manipulation of Cell Adhesion, Release, and Differentiation. *Angew. Chemie - Int. Ed.* **58**, 14519–14523 (2019).

53. Davis, K. A., Burke, K. A., Mather, P. T. & Henderson, J. H. Dynamic cell behavior on shape memory polymer substrates. *Biomaterials* **32**, 2285–2293 (2011).

54. Corbin, E. A. *et al.* Tunable and Reversible Substrate Stiffness Reveals a Dynamic Mechanosensitivity of Cardiomyocytes. *ACS Appl. Mater. Interfaces* **11**, 20603–20614 (2019).

55. Young, J. L. & Engler, A. J. Hydrogels with time-dependent material properties enhance cardiomyocyte differentiation in vitro. *Biomaterials* **32**, 1002–1009 (2011).

56. Mengsteab, P. Y. *et al.* Spatiotemporal control of cardiac anisotropy using dynamic nanotopographic cues. *Biomaterials* **86**, 1–10 (2016).

57. Beblo, R. V. & Weiland, L. M. Demonstration of a multiscale modeling technique: Prediction of the stress-strain response of light activated shape memory polymers. *Smart Mater. Struct.* **19**, (2010).

58. Wang, C. C., Huang, W. M., Ding, Z., Zhao, Y. & Purnawali, H. Cooling-/water-responsive shape memory hybrids. *Compos. Sci. Technol.* **72**, 1178–1182 (2012).

59. Leng, J., Lv, H., Liu, Y. & Du, S. Synergic effect of carbon black and short carbon fiber on shape memory polymer actuation by electricity. *J. Appl. Phys.* **104**, 1–5 (2008).

60. Kim, D.-H. *et al.* Nanoscale cues regulate the structure and function of macroscopic cardiac tissue constructs. *Proc. Natl. Acad. Sci.* **107**, 565–570 (2010).

61. Uto, K., Ebara, M. & Aoyagi, T. Temperature-responsive poly(ε-caprolactone) cell culture platform with dynamically tunable nano-roughness and elasticity for control of

myoblast morphology. *Int. J. Mol. Sci.* **15**, 1511–1524 (2014).

62. Rianna, C. *et al.* Reversible Holographic Patterns on Azopolymers for Guiding Cell Adhesion and Orientation. *ACS Appl. Mater. Interfaces* **7**, 16984–16991 (2015).

63. Case, L. B. *et al.* Molecular mechanism of vinculin activation and nanoscale spatial organization in focal adhesions. *Nat. Cell Biol.* **17**, 880–892 (2015).

64. Hirata, H., Tatsumi, H. & Sokabe, M. Mechanical forces facilitate actin polymerization at focal adhesions in a zyxin-dependent manner. *J. Cell Sci.* **121**, 2795–2804 (2008).

65. Frey, M. T., Tsai, I. Y., Russell, T. P., Hanks, S. K. & Wang, Y. L. Cellular responses to substrate topography: Role of myosin II and focal adhesion kinase. *Biophys. J.* **90**, 3774–3782 (2006).

66. Ren, X. D. *et al.* Focal adhesion kinase suppresses Rho activity to promote focal adhesion. *J. Cell Sci.* **113**, 3673–3678 (2000).

67. Slack-Davis, J. K. *et al.* Cellular characterization of a novel focal adhesion kinase inhibitor. *J. Biol. Chem.* **282**, 14845–14852 (2007).

68. Porter, G. A., Dmytrenko, G. M., Winkelmann, J. C. & Bloch, R. J. Dystrophin colocalizes with β-spectrin in distinct subsarcolemmal domains in mammalian skeletal muscle. *J. Cell Biol.* **117**, 997–1005 (1992).

69. Hamadi, A. *et al.* Regulation of focal adhesion dynamics and disassembly by phosphorylation of FAK at tyrosine 397. **397**, (2005).

70. Zhong, W., Li, Y. & Li, L. YAP-mediated regulation of the chondrogenic phenotype in response to matrix elasticity. 587–595 (2013). doi:10.1007/s10735-013-9502-y

71. Anastasi, G. *et al.* Costameric proteins in human skeletal muscle during muscular inactivity. *J. Anat.* **213**, 284–295 (2008).

72. Israeli-Rosenberg, S., Manso, A. M., Okada, H. & Ross, R. S. Integrins and integrin-associated proteins in the cardiac myocyte. *Circ. Res.* **114**, 572–586 (2014).

# Vita

**Huaiyu Shi** **hshi14@syr.edu**

**Education**

**Syracuse University, Syracuse NY** M.S. August 2018 to July 2020

Thesis Title "Cell-adhesion Activities Responding to Nano-Dynamic Substrate"

Thesis Advisor: Dr. Zhen Ma

**Tianjin University, Tianjin China** M.S. September 2015 to July 2018

Thesis Title "Effects of *LcAPX* on plant cadmium resistance and optimizing of rice callus culture condition"

Thesis Advisor: Dr. Gang Wang

**Tianjin Normal University, Tianjin China** B.S. September 2011 to July 2015

**Publications and Presentations**

Sun, S., **Shi, H. (Co-first author)**, Moore, S., Wang, C., Ash-Shakoor, A., Mather, P. T., … Ma, Z. (2020). Progressive Myofibril Reorganization of Human Cardiomyocytes on a Dynamic Nanotopographic Substrate. *ACS Applied Materials and Interfaces,* 12(19), 21450–21462. https://doi.org/10.1021/acsami.0c03464

**Shi, H.**, Sun S., Moore S., Wang C., Henderson J., Ma Z. Cell-adhesion Activities Responding to Nano-Dynamic Substrate. *Stevenson Biomaterials Lecture Series, Poster,* Syracuse, NY 2020.